Isogeometric Analysis of the Navier–Stokes equations with Taylor–Hood B-spline elements

Babak S. Hosseini^{a,*}, Matthias Möller^b, Stefan Turek^a

^aTU Dortmund, Institute of Applied Mathematics (LS III), Vogelpothsweg 87, 44227 Dortmund, Germany
^bDelft University of Technology, Delft Institute of Applied Mathematics, Mekelweg 4, 2628 CD Delft, The

Netherlands

Abstract

This paper presents our numerical results of the application of Isogeometric Analysis (IGA) to the velocity–pressure formulation of the steady state as well as to the unsteady incompressible Navier–Stokes equations. For the approximation of the velocity and pressure fields, LBB compatible B-spline spaces are used which can be regarded as smooth generalizations of Taylor–Hood pairs of finite element spaces. The single-step θ -scheme is used for the discretization in time. The lid-driven cavity flow, in addition to its regularized version and flow around cylinder, are considered in two dimensions as model problems in order to investigate the numerical properties of the scheme.

Keywords: Isogeometric Analysis, Isogeometric finite elements, B-splines, NURBS, Fluid mechanics, Navier—Stokes equations, Lid-driven cavity flow, Flow around cylinder.

1. Introduction

The Isogeometric Analysis technique, developed by Hughes et al. [7], is a powerful numerical technique aiming to bridge the gap between the worlds of computer-aided engineering (CAE) and computer-aided design (CAD). It combines the benefits of Finite Element Analysis (FEA) with the ability of an exact representation of complex computational domains via an elegant mathematical description in the form of uni-, bi- or trivariate non-uniform rational B-splines. Non-Uniform Rational B-splines (NURBS) are the de facto industry standard when it comes to modeling complex geometries, while FEA is a numerical approximation technique that is widely used in computational mechanics.

NURBS and FEA utilize basis functions for the representation of geometry and approximation of field variables, respectively. In order to close the gap between the two technologies, Isogeometric Analysis adopts the B-spline, NURBS or T-spline (see [7]) geometry as the computational domain and utilizes its basis functions to construct both trial and test spaces in the discrete variational formulation of differential problems. The usage of these functions allows the construction of approximation spaces exhibiting higher regularity ($C^{\geq 0}$) which – depending on the problem to be solved – may be beneficial compared to standard finite element

^{*}Corresponding author

Email addresses: babak.hosseini@math.tu-dortmund.de (Babak S. Hosseini), m.moller@tudelft.nl (Matthias Möller), stefan.turek@math.tu-dortmund.de (Stefan Turek)

spaces. For instance, Cottrell, Hughes and Reali showed in their study of refinement and continuity in isogeometric structural analysis [8] that increased smoothness leads to a significant increase in accuracy for the problems of structural vibrations over the classical C^0 continuous p-method of FEA. Isogeometric Analysis has been successfully applied to high order partial differential equations (PDEs) from a wide range of fields of computational mechanics. In fact, primal variational formulations of high order PDEs such as Navier–Stokes–Korteweg (3rd order spatial derivatives) or Cahn–Hilliard (4th order spatial derivatives) require piecewise smooth and globally C^1 continuous basis functions. Note that the number of finite elements possessing C^1 continuity and being applicable to complex geometries is already very limited in two dimensions [13, 14]. The Isogeometric Analysis technology features a unique combination of attributes, namely, superior accuracy on degree of freedom basis, robustness, two- and three-dimensional geometric flexibility, compact support, and the possibility for $C^{\geq 0}$ continuity [7].

This article is all about the application and assessment of the Isogeometric Analysis approach to fluid flows with respect to well known benchmark problems. We present our numerical results for the lid-driven cavity flow problem (including its regularized version) using different B-spline approximation spaces, and compare them to reference results from literature. Moreover, in addition to comparisons with classical references, we will whenever feasible take into consideration the results of two recently published articles [9, 21] on the application of Galerkin-based IGA to the cavity flow problem. The analysis presented in [21] is based on a scalar stream function formulation of the Navier–Stokes equations, while [9] uses divergence-conforming B-splines which may be interpreted as smooth generalizations of Raviart–Thomas elements. We extend this Galerkin IGA-based row of results for cavity flow with data obtained from the application of smooth generalizations of Taylor–Hood elements. Despite the fact that investigations of lid-driven cavity type model problems do not necessarily reflect the current spirit of time, they are nonetheless a natural first choice in computational fluid dynamics when it comes to assessing the properties of a novel numerical technique.

Subsequent to lid-driven cavity, we eventually proceed to present and assess approximated physical quantities such as the drag and lift coefficients obtained for the flow around cylinder benchmark, whereby a multi-patch discretization approach is adopted. For the scenarios addressed, Isogeometric Analysis is applied to the steady-state as well as to the transient incompressible Navier—Stokes equations. For the equations under consideration are of nonlinear nature, we decided to provide a rather detailed insight concerning their treatment. The efficient solution of the discretized system of equations using iterative solution techniques such as, for instance, multigrid is not addressed in this paper. Preliminary research results are underway and will be presented in a forthcoming publication. In this numerical study, all systems of equations have been solved with a direct solver.

The outline of this paper is as follows: Section 2 is devoted to the introduction of the univariate and the multivariate (tensor product) B-spline and NURBS (non-uniform rational B-spline) basis functions, their related spaces, and the NURBS geometrical map F. This presentation is quite brief and notationally oriented. A more complete introduction to NURBS and Isogeometric Analysis can be found in [3, 7, 18]. Section 3 formalizes Taylor–Hood like discrete approximation spaces being used in different peculiarities throughout this article. Section 4 is dedicated to the presentation of the governing equations and their variational forms. The numerical results are showcased in Section 5. In particular, in Sections 5.2 and

5.4, numerical results of Isogeometric Analysis of lid-driven cavity flow and flow around cylinder are presented and compared with reference results from literature. Section 6 is dedicated to a short summary in addition to drawn conclusions.

2. Preliminaries

In order to fix the notation and for the sake of completeness, this section presents a brief overview of B-spline/NURBS basis functions and their corresponding spaces utilized in Isogeometric Analysis.

Galerkin-based Isogeometric Analysis adopts spline (B-spline/NURBS, etc.) basis functions for analysis as well as for the description of the geometry (computational domain). Just like in FEA, a discrete approximation space — based on the span of the basis functions in charge — is constructed and eventually used in the framework of a Galerkin procedure for the numerical approximation of the solution of partial differential equations. ¹

Recalling reference $(\tilde{\Omega})$ and physical domains (Ω) in FEA, using B-splines/NURBS, one additional domain – the parametric spline domain $(\hat{\Omega})$ – needs to be considered as well (see Fig. 1). We follow this requirement and present an insight in the traits of spline-based discrete approximation spaces in the sequel.

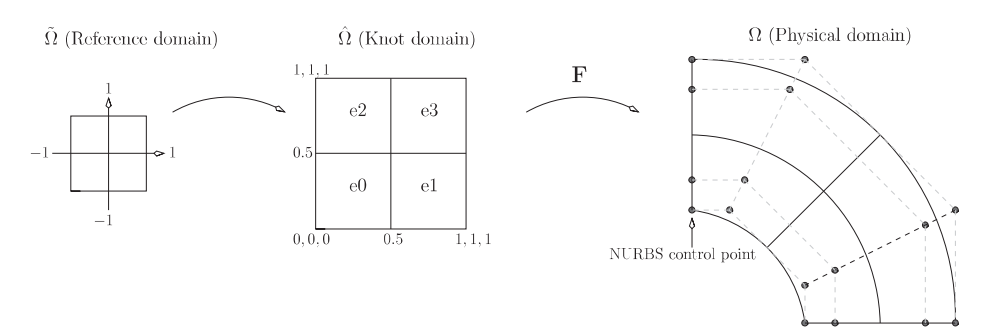


Figure 1: Domains involved in Isogeometric Analysis. Left: Reference domain used to evaluate integrals; Center: Exemplary parametric spline domain with knot vectors $\Xi_u = \Xi_v := \{0, 0, 0, 0.5, 1, 1, 1\}$ defining four elements $(e0, \ldots, e3)$, two in each parametric direction. Right: Image of the knot space coordinates under the parameterization \mathbf{F} .

Given two positive integers p and n, we introduce the ordered knot vector

$$\Xi := \{ 0 = \xi_1, \xi_2, \dots, \xi_m = 1 \}, \tag{1}$$

whereby repetitions of the m = n + p + 1 knots ξ_i are allowed: $\xi_1 \leq \xi_2 \leq \cdots \leq \xi_m$. Note that in (1) the values of Ξ are normalized to the range [0, 1] merely for the sake of clarity and not restricted in range otherwise. Besides, we assume that Ξ is an open knot vector, that is, the first and last knots have multiplicity p + 1:

$$\Xi = \{\underbrace{0, \dots, 0}_{p+1}, \xi_{p+2}, \dots, \xi_{m-p-1}, \underbrace{1, \dots, 1}_{p+1}\}.$$

¹ We point out on a side note that IGA is not restricted to the Galerkin framework and has as a matter of fact been successfully used with Collocation techniques as well, see for instance [2, 20].

Let the (univariate) B-spline basis functions of degree p (order p+1) be denoted by $B_{i,p}(\xi)$, for $i=1,\ldots,n$. Then, the *i*th B-spline basis function is a piecewise polynomial function and it is recursively defined by the Cox-de Boor recursion formula:

$$B_{i,0}(\xi) = \begin{cases} 1, & \text{if } \xi_i \le \xi < \xi_{i+1} \\ 0, & \text{otherwise} \end{cases}$$

$$B_{i,p}(\xi) = \frac{\xi - \xi_i}{\xi_{i+p} - \xi_i} B_{i,p-1}(\xi) + \frac{\xi_{i+p+1} - \xi}{\xi_{i+p+1} - \xi_{i+1}} B_{i+1,p-1}(\xi), \quad p > 0.$$
(2)

At knot ξ_i the basis functions have $\alpha := p - r_i$ continuous derivatives, where r_i denotes the multiplicity of knot ξ_i . The quantity α is bounded from below and above by $-1 \le \alpha \le p - 1$. Thus, the maximum multiplicity allowed is $r_i = p + 1$, rendering the basis functions at ξ_i discontinuous as it is the case at the boundaries of the interval.

Each basis function $B_{i,p}$ is non-negative over its support (ξ_i, ξ_{i+p+1}) . The interval (ξ_i, ξ_{i+1}) is referred to as a knot span or element in IGA speak. Moreover, the B-spline basis functions are linearly independent and constitute a partition of unity, that is, $\sum_{i=1}^{n} B_{i,p}(\xi) = 1$ for all $\xi \in [0,1]$. Figure 2 illustrates the basis functions of degree 2 of an exemplary knot vector exhibiting different levels of continuity. Due to the recursive definition (2), the derivative of

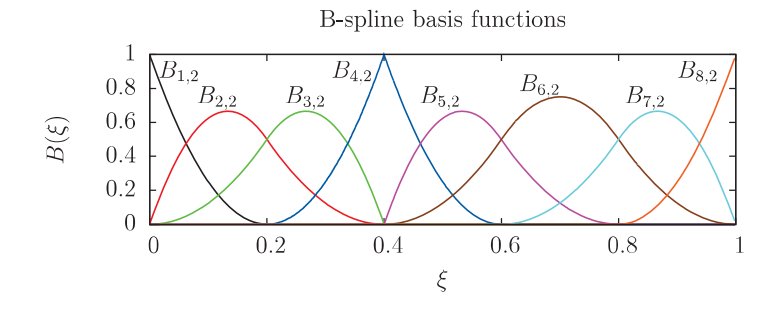


Figure 2: Plot of B-spline basis functions of degree 2 corresponding to the open knot vector $\Xi := \{0, 0, 0, 0.2, 0.4, 0.4, 0.6, 0.8, 1, 1, 1\}$. Due to the open knot vector trait, the first and last basis functions are interpolatory, that is, they take the value 1 at the first and last knot. At an interior knot ξ_i the continuity is C^{p-r_i} with r_i denoting the multiplicity of knot ξ_i . Due to the multiplicity $r_5 = 2$ of knot $\xi_5 = 0.4$, the continuity of the basis functions across this parametric point is $C^{p-2} = C^0$, while at the other interior knots the continuity is $C^{p-1} = C^1$.

the *i*th B-spline basis function is given by

$$B'_{i,p}(\xi) = \frac{p}{\xi_{i+p} - \xi_i} B_{i,p-1}(\xi) - \frac{p}{\xi_{i+p+1} - \xi_{i+1}} B_{i+1,p-1}(\xi)$$
(3)

which is a combination of lower order B-spline functions. The generalization to higher derivatives is straightforward by simply differentiating each side of the above relation.

Univariate rational B-spline basis functions are obtained by augmenting the set of B-spline basis functions with weights w_i and defining:

$$R_{i,p}(\xi) = \frac{B_{i,p}(\xi)w_i}{W(\xi)}, \qquad W(\xi) = \sum_{j=1}^n B_{j,p}(\xi)w_j.$$
 (4)

Its derivative is obtained by simply applying the quotient rule. By setting all weighting coefficients equal to one it follows that B-splines are just a special case of NURBS.

The space of B-splines of degree p and regularity α determined by the knot vector Ξ is spanned by the basis functions $B_{i,p}$ and will be denoted by

$$S_{\alpha}^{p} \equiv S_{\alpha}^{p}(\Xi, p) := \operatorname{span}\{B_{i,p}\}_{i=1}^{n}.$$
(5)

Analogously, we define the space spanned by rational B-spline basis functions as

$$\mathcal{N}_{\alpha}^{p} \equiv \mathcal{N}_{\alpha}^{p}(\Xi, p, w) := \operatorname{span}\{R_{i,p}\}_{i=1}^{n}.$$
 (6)

The definition of univariate B-spline spaces can readily be extended to higher dimensions. To this end, we consider d knot vectors Ξ_{β} , $1 \leq \beta \leq d$ and an open parametric domain $(0,1)^d \in \mathbb{R}^d$. The knot vectors Ξ_{β} partition the parametric domain $(0,1)^d$ into d-dimensional open knot spans, or elements, and thus yield a mesh \mathcal{Q} being defined as

$$Q \equiv Q(\Xi_1, \dots, \Xi_d) := \{ Q = \bigotimes_{\beta=1}^d (\xi_{i,\beta}, \xi_{i+1,\beta}) \mid Q \neq \emptyset, \ 1 \le i \le m_\beta \}$$
 (7)

For an element $Q \in \mathcal{Q}$, we set $h_Q = \operatorname{diam}(Q)$, and define the global mesh size $h = \max\{h_Q, Q \in \mathcal{Q}\}$. We define the tensor product B-spline and NURBS basis functions as

$$B_{i_1,\dots,i_d} := B_{i_1,1} \otimes \dots \otimes B_{i_d,d}, \quad i_1 = 1,\dots,n_1, \quad i_d = 1,\dots,n_d$$
 (8)

and

$$R_{i_1,\dots,i_d} := R_{i_1,1} \otimes \dots \otimes R_{i_d,d}, \quad i_1 = 1,\dots,n_1, \quad i_d = 1,\dots,n_d,$$
 (9)

respectively. Then, the tensor product B-spline and NURBS spaces, spanned by the respective basis functions, are defined as

$$S_{\alpha_1,\dots,\alpha_d}^{p_1,\dots,p_d} \equiv S_{\alpha_1,\dots,\alpha_d}^{p_1,\dots,p_d}(\mathcal{Q}) := S_{\alpha_1}^{p_1} \otimes \dots \otimes S_{\alpha_d}^{p_d} = \operatorname{span}\{B_{i_1\dots i_d}\}_{i_1=1,\dots,i_d=1}^{n_1,\dots,n_d}$$
(10)

and

$$\mathcal{N}_{\alpha_1,\dots,\alpha_d}^{p_1,\dots,p_d} \equiv \mathcal{N}_{\alpha_1,\dots,\alpha_d}^{p_1,\dots,p_d}(\mathcal{Q}) := \mathcal{N}_{\alpha_1}^{p_1} \otimes \dots \otimes \mathcal{N}_{\alpha_d}^{p_d} = \operatorname{span}\{R_{i_1\dots i_d}\}_{i_1=1,\dots,i_d=1}^{n_1,\dots,n_d}, \tag{11}$$

respectively. The space $S_{\alpha_1,\ldots,\alpha_d}^{p_1,\ldots,p_d}$ is fully characterized by the mesh \mathcal{Q} , the degrees p_1,\ldots,p_d of basis functions and their continuities α_1,\ldots,α_d . The minimum regularity/continuity of the space is $\alpha:=\min\{\alpha_i,i\in(1,d)\}$.

For a representation of the elements in the physical domain Ω , the mesh \mathcal{Q} is mapped to the physical space via a NURBS geometrical map $\mathbf{F}: \hat{\Omega} \to \Omega$

$$\mathbf{F} = \sum_{i_1=1}^{n_1} \cdots \sum_{i_d=1}^{n_d} R_{i_1}(\xi_{i_1}) \dots R_{i_d}(\xi_{i_d}) \mathbf{P}_{i_1,\dots,i_d}$$
(12)

yielding a mesh \mathcal{K} , with

$$\mathcal{K} = \mathbf{F}(Q) := \{ \mathbf{F}(\boldsymbol{\xi}) | \boldsymbol{\xi} \in Q \}. \tag{13}$$

With the definition of \mathbf{F} in hand, the space \mathcal{V} of NURBS basis functions on Ω , being the push-forward of the space \mathcal{N} , is defined as

$$\mathcal{V}_{\alpha_1,\dots,\alpha_d}^{p_1,\dots,p_d} \equiv \mathcal{V}_{\alpha_1,\dots,\alpha_d}^{p_1,\dots,p_d}(\mathcal{K}) := \mathcal{V}_{\alpha_1}^{p_1} \otimes \dots \otimes \mathcal{V}_{\alpha_d}^{p_d} = \operatorname{span}\{R_{i_1\dots i_d} \circ \mathbf{F}^{-1}\}_{i_1=1,\dots,i_d=1}^{n_1,\dots,n_d}$$
(14)

In equation (12), **P**, denotes a homogeneous NURBS control point uniquely addressed in the NURBS tensor product mesh by its indices.

We assume that the parameterization \mathbf{F} is invertible, with smooth inverse, on each element $Q \in \mathcal{Q}$. A mesh stack $\{\mathcal{Q}_h\}_{h \leq h_0}$, with affiliated spaces, can be constructed via knot insertion as described, e.g., in [7] from an initial coarse mesh \mathcal{Q}_0 , with the global mesh size h pointing to a refinement level index.

3. Discrete approximation spaces

For an Isogeometric Analysis-based approximation of the unknowns of the PDEs considered in this article (see Section 4), suitable B-spline or NURBS spaces, as defined in Section 2, need to be specified. For the approximation of the velocity and pressure functions, we use LBB-stable Taylor–Hood-like B-spline space pairs $\hat{\mathbf{V}}_h^{TH}/\hat{Q}_h^{TH}$ [6], being defined in the parametric domain $\hat{\Omega}$ as

$$\hat{\mathbf{V}}_{h}^{TH} \equiv \hat{\mathbf{V}}_{h}^{TH}(\mathbf{p}, \boldsymbol{\alpha}) = \boldsymbol{\mathcal{S}}_{\alpha_{1}, \alpha_{2}}^{p_{1}+1, p_{2}+1} = \boldsymbol{\mathcal{S}}_{\alpha_{1}, \alpha_{2}}^{p_{1}+1, p_{2}+1} \times \boldsymbol{\mathcal{S}}_{\alpha_{1}, \alpha_{2}}^{p_{1}+1, p_{2}+1},
\hat{Q}_{h}^{TH} \equiv \hat{Q}_{h}^{TH}(\mathbf{p}, \boldsymbol{\alpha}) = \boldsymbol{\mathcal{S}}_{\alpha_{1}, \alpha_{2}}^{p_{1}, p_{2}}.$$
(15)

With the definition of finite dimensional spaces $\hat{\mathbf{V}}_h^{TH}$ and \hat{Q}_h^{TH} in hand, we proceed to construct the corresponding spaces \mathbf{V}_h^{TH} and Q_h^{TH} in the physical domain Ω . Taylor–Hood spaces $\hat{\mathbf{V}}_h^{TH}/\hat{Q}_h^{TH}$ can be mapped to the physical domain via a component-wise mapping [6] using the parameterization $\mathbf{F}: \hat{\Omega} \to \Omega$, i.e.

$$\mathbf{V}_{h}^{TH} = \{ \mathbf{v} : \mathbf{v} \circ \mathbf{F} \in \hat{\mathbf{V}}_{h}^{TH} \}, \qquad Q_{h}^{TH} = \{ q : q \circ \mathbf{F} \in \hat{Q}_{h}^{TH} \}.$$
 (16)

Note that these spaces may be alternatively set up to use NURBS instead of B-spline basis functions.

Throughout this article, whenever a specific discrete B-spline or NURBS approximation space is addressed, we introduce – for the sake of brevity – the convention to refer to its presentation w.r.t. the parametric domain $\hat{\Omega}$, as shown in (15).

4. Governing equations

For stationary flow scenarios considered in this article, the governing equations to be solved are the steady-state incompressible Navier–Stokes equations represented in strong form as

$$-\nu \nabla^2 \mathbf{v} + (\mathbf{v} \cdot \nabla) \mathbf{v} + \nabla p = \mathbf{b} \quad \text{in } \Omega, \tag{17a}$$

$$\nabla \cdot \boldsymbol{v} = 0 \quad \text{in } \Omega, \tag{17b}$$

$$\mathbf{v} = \mathbf{v}_D \quad \text{on } \Gamma_D,$$
 (17c)

$$-p\mathbf{n} + \nu(\mathbf{n} \cdot \nabla)\mathbf{v} = \mathbf{t} \quad \text{on } \Gamma_N, \tag{17d}$$

where $\Omega \subset \mathbb{R}^2$ is a bounded domain, ρ is the density, μ represents the dynamic viscosity, $\nu = \mu/\rho$ is the kinematic viscosity, $p = P/\rho$ denotes the normalized pressure, \boldsymbol{b} is the body force term, \boldsymbol{v}_D is the value of the velocity Dirichlet boundary conditions on the Dirichlet boundary Γ_D , \boldsymbol{t} is the prescribed traction force on the Neumann boundary Γ_N , and \boldsymbol{n} is the

outward unit normal vector on the boundary. The kinematic viscosity and the density of the fluid are assumed to be constant. The first and second equations in (17) are the momentum and continuity equations, respectively.

Their continuous mixed variational formulation reads: Find $\boldsymbol{v} \in \mathcal{H}^1_{\Gamma_D}(\Omega)$ and $p \in$ $\mathcal{L}_2(\Omega)/\mathbb{R}$ such that for all $(\boldsymbol{w},q) \in \mathcal{H}_0^1(\Omega) \times \mathcal{L}_2(\Omega)/\mathbb{R}$ it holds

$$\begin{cases}
a(\boldsymbol{w}, \boldsymbol{v}) + c(\boldsymbol{v}; \boldsymbol{w}, \boldsymbol{v}) + b(\boldsymbol{w}, p) = (\boldsymbol{w}, \boldsymbol{b}) + (\boldsymbol{w}, \boldsymbol{t})_{\Gamma_N} \\
b(\boldsymbol{v}, q) = 0,
\end{cases}$$
(18)

where \mathcal{L}_2 and \mathcal{H}^1 are Sobolev spaces as defined in [1].

Replacement of the linear-, bilinear- and trilinear forms with their respective definitions and application of integration by parts to (18) yields

$$\underbrace{\nu \int_{\Omega} \nabla \boldsymbol{w} : \nabla \boldsymbol{v} \, d\Omega}_{a(\boldsymbol{w}, \boldsymbol{v})} + \underbrace{\int_{\Omega} \boldsymbol{w} \cdot \boldsymbol{v} \cdot \nabla \boldsymbol{v} \, d\Omega}_{c(\boldsymbol{v}; \boldsymbol{w}, \boldsymbol{v})} - \underbrace{\int_{\Omega} \nabla \cdot \boldsymbol{w} p \, d\Omega}_{b(\boldsymbol{w}, p)} - \underbrace{\int_{\Omega} q \nabla \cdot \boldsymbol{v} \, d\Omega}_{b(\boldsymbol{v}, q)} = \underbrace{\underbrace{\int_{\Omega} \boldsymbol{w} \cdot \boldsymbol{b} \, d\Omega}_{c(\boldsymbol{v}; \boldsymbol{w}, \boldsymbol{v})} + \underbrace{\int_{\Gamma_{N}} \nu \boldsymbol{w} \cdot (\nabla \boldsymbol{v} \cdot \boldsymbol{n}) \, d\Gamma_{N} - \int_{\Gamma_{N}} p \boldsymbol{w} \cdot \boldsymbol{n} \, d\Gamma_{N}}_{(\boldsymbol{w}, \boldsymbol{t})_{\Gamma_{N}}} \tag{19}}$$

A downcast of the variational formulation (18) to the discrete level gives rise to the problem statement

$$\begin{cases}
\operatorname{Find} \ \boldsymbol{v}^{h} \in \boldsymbol{\mathcal{H}}_{\Gamma_{D}}^{1}(\Omega) \cap \mathbf{V}_{h}^{TH} \text{ and } p^{h} \in \mathcal{L}_{2}(\Omega)/\mathbb{R} \cap Q_{h}^{TH}, \text{ such that} \\
\forall (\boldsymbol{w}^{h}, q^{h}) \in \boldsymbol{\mathcal{H}}_{0}^{1}(\Omega) \cap \mathbf{V}_{h}^{TH} \times \mathcal{L}_{2}(\Omega)/\mathbb{R} \cap Q_{h}^{TH} \\
a(\boldsymbol{w}^{h}, \boldsymbol{v}^{h}) + c(\boldsymbol{v}^{h}; \boldsymbol{w}^{h}, \boldsymbol{v}^{h}) + b(\boldsymbol{w}^{h}, p^{h}) = (\boldsymbol{w}^{h}, \boldsymbol{b}^{h}) + (\boldsymbol{w}^{h}, \boldsymbol{t}^{h})_{\Gamma_{N}} \\
b(\boldsymbol{v}^{h}, q^{h}) = 0,
\end{cases} \tag{20}$$

with superscript h dubbing the mesh family index.

In addition to the stationary flow around a circular obstacle model problem, we also consider its unsteady counterpart (see Section 5.4). In the latter case, the unsteady incompressible Navier–Stokes equations, defined as

$$\frac{\partial \boldsymbol{v}}{\partial t} - \nu \nabla^2 \boldsymbol{v} + (\boldsymbol{v} \cdot \nabla) \boldsymbol{v} + \nabla p = \boldsymbol{b} \quad \text{in } \Omega \times]0, T[,$$

$$\nabla \cdot \boldsymbol{v} = 0 \quad \text{in } \Omega \times]0, T[,$$
(21a)

$$\nabla \cdot \boldsymbol{v} = 0 \qquad \text{in } \Omega \times]0, T[, \tag{21b}$$

$$\mathbf{v} = \mathbf{v}_D \quad \text{on } \Gamma_D \times]0, T[,$$
 (21c)

$$-p\mathbf{n} + \nu(\mathbf{n} \cdot \nabla)\mathbf{v} = \mathbf{t} \qquad \text{on } \Gamma_N \times]0, T[, \tag{21d}$$

$$\boldsymbol{v}(\boldsymbol{x},0) = \boldsymbol{v}_0(\boldsymbol{x}) \text{ in } \Omega,$$
 (21e)

are solved in time, whereby the initial condition is required to satisfy $\nabla \cdot v_0 = 0$. The corresponding variational problem reads: Find $\boldsymbol{v}(\boldsymbol{x},t) \in \boldsymbol{\mathcal{H}}_{\Gamma_D}^{1}(\Omega) \times]0, T[$ and $p(\boldsymbol{x},t) \in \mathcal{L}_2(\Omega) \times]0, T[$, such that for all $(\boldsymbol{w},q) \in \mathcal{H}^1_{\Gamma_0}(\Omega) \times \mathcal{L}_2(\Omega)/\mathbb{R}$ it holds

$$\begin{cases} (\boldsymbol{w}, \boldsymbol{v}_t) + a(\boldsymbol{w}, \boldsymbol{v}) + c(\boldsymbol{v}; \boldsymbol{w}, \boldsymbol{v}) + b(\boldsymbol{w}, p) = (\boldsymbol{w}, \boldsymbol{b}) + (\boldsymbol{w}, \boldsymbol{t})_{\Gamma_N} \\ b(\boldsymbol{v}, q) = 0 \end{cases}$$
(22)

Analogously, the semi-discretized counterpart of the variational formulation (22) reads:

$$\begin{cases}
\operatorname{Find} \ \boldsymbol{v}^{h} \in \boldsymbol{\mathcal{H}}_{\Gamma_{D}}^{1}(\Omega) \cap \mathbf{V}_{h}^{TH} \times]0, T[\text{ and } p^{h} \in \mathcal{L}_{2}(\Omega)/\mathbb{R} \cap Q_{h}^{TH} \times]0, T[\text{ such that} \\
\forall (\boldsymbol{w}^{h}, q^{h}) \in \boldsymbol{\mathcal{H}}_{0}^{1}(\Omega) \cap \mathbf{V}_{h}^{TH} \times \mathcal{L}_{2}(\Omega)/\mathbb{R} \cap Q_{h}^{TH} \\
(\boldsymbol{w}^{h}, \boldsymbol{v}_{t}^{h}) + a(\boldsymbol{w}^{h}, \boldsymbol{v}^{h}) + c(\boldsymbol{v}^{h}; \boldsymbol{w}^{h}, \boldsymbol{v}^{h}) + b(\boldsymbol{w}^{h}, p^{h}) = (\boldsymbol{w}^{h}, \boldsymbol{b}^{h}) + (\boldsymbol{w}^{h}, \boldsymbol{t}^{h})_{\Gamma_{N}} \\
b(\boldsymbol{v}^{h}, q^{h}) = 0
\end{cases} \tag{23}$$

Since the nonlinear nature of the Navier–Stokes equations involves a great deal of complexity, we deliver in Section 4.1 an insight into the handling of the nonlinearity aspect.

4.1. Treatment of nonlinearity

The treatment of nonlinearity is showcased for the steady Navier–Stokes system as presented in equation (17). This choice is motivated by the desire to keep this section as brief as possible. Note that the same principles for the treatment of nonlinearity apply to the unsteady Navier–Stokes system as well.

Let the nonlinear system (17) be presented in operator form as

$$\mathcal{L}(\boldsymbol{u}) = \boldsymbol{b} \quad \text{with } \boldsymbol{u} = (\boldsymbol{v}, p), \tag{24}$$

and let it be disassembled as $\mathcal{L} = \mathcal{L}_A \oplus \mathcal{L}_V \oplus \mathcal{L}_G \oplus \mathcal{L}_D$, with operators $\mathcal{L}_A = \boldsymbol{v} \cdot \nabla \boldsymbol{v}$, $\mathcal{L}_V = -\nu \nabla^2 \boldsymbol{v}$, $\mathcal{L}_G = \nabla p$ and $\mathcal{L}_D = \nabla \cdot \boldsymbol{v}$.

In order to solve equation (24), an iterative procedure is required which, starting from an initial guess for the unknowns, linearizes in every relaxation step the nonlinear system based on the current solution u^n , and eventually solves the resulting system of linear equations. The iteration is advanced until a stopping criteria such as convergence is achieved.

Since the only nonlinear term in equation (24) is given by the advection operator \mathcal{L}_A , we linearize the latter via a generalized Taylor expansion of \mathcal{L}_A about the current iterate of the velocity function \mathbf{v}^n and ignore higher order terms $O(|\delta \mathbf{v}|^2)$. A Newton linearization of \mathcal{L}_A is derived as:

$$\mathcal{L}_{A}(\boldsymbol{v}) = \mathcal{L}_{A}(\boldsymbol{v}^{n}) + \frac{d\mathcal{L}_{A}(\boldsymbol{v}^{n} + \epsilon\delta\boldsymbol{v})}{d\epsilon} \bigg|_{\epsilon=0} + O(|\delta\boldsymbol{v}|^{2})$$

$$\approx \boldsymbol{v}^{n} \cdot \nabla \boldsymbol{v}^{n} + \frac{d[(\boldsymbol{v}^{n} + \epsilon\delta\boldsymbol{v}) \cdot \nabla(\boldsymbol{v}^{n} + \epsilon\delta\boldsymbol{v})]}{d\epsilon} \bigg|_{\epsilon=0}$$

$$= \boldsymbol{v}^{n} \cdot \nabla \boldsymbol{v}^{n} + \frac{d[\boldsymbol{v}^{n} \cdot \nabla(\boldsymbol{v}^{n} + \epsilon\delta\boldsymbol{v}) + \epsilon\delta\boldsymbol{v} \cdot \nabla(\boldsymbol{v}^{n} + \epsilon\delta\boldsymbol{v})]}{d\epsilon} \bigg|_{\epsilon=0}$$

$$= \boldsymbol{v}^{n} \cdot \nabla \boldsymbol{v}^{n} + \frac{d[\boldsymbol{v}^{n} \cdot \nabla\boldsymbol{v}^{n} + \boldsymbol{v}^{n} \cdot \nabla\epsilon\delta\boldsymbol{v} + \epsilon\delta\boldsymbol{v} \cdot \nabla\boldsymbol{v}^{n} + \epsilon^{2}\delta\boldsymbol{v} \cdot \nabla\delta\boldsymbol{v}]}{d\epsilon} \bigg|_{\epsilon=0}$$

$$= \boldsymbol{v}^{n} \cdot \nabla \boldsymbol{v}^{n} + \boldsymbol{v}^{n} \cdot \nabla\delta\boldsymbol{v} + \delta\boldsymbol{v} \cdot \nabla\boldsymbol{v}^{n} = \boldsymbol{v}^{n} \cdot \nabla\boldsymbol{v}^{n} + \boldsymbol{v}^{n} \cdot \nabla(\boldsymbol{v} - \boldsymbol{v}^{n}) + (\boldsymbol{v} - \boldsymbol{v}^{n}) \cdot \nabla\boldsymbol{v}^{n}$$

$$= \boldsymbol{v}^{n} \cdot \nabla\boldsymbol{v}^{n} + \boldsymbol{v}^{n} \cdot \nabla\delta\boldsymbol{v} + \delta\boldsymbol{v} \cdot \nabla\boldsymbol{v}^{n} + \boldsymbol{v}^{n} \cdot \nabla(\boldsymbol{v} - \boldsymbol{v}^{n}) + (\boldsymbol{v} - \boldsymbol{v}^{n}) \cdot \nabla\boldsymbol{v}^{n}$$

$$= \boldsymbol{v}^{n} \cdot \nabla\boldsymbol{v}^{n} + \boldsymbol{v}^{n} \cdot \nabla\boldsymbol{v} - \boldsymbol{v}^{n} \cdot \nabla\boldsymbol{v}^{n} + \boldsymbol{v} \cdot \nabla\boldsymbol{v}^{n} - \boldsymbol{v}^{n} \cdot \nabla\boldsymbol{v}^{n}$$

$$= \boldsymbol{v}^{n} \cdot \nabla\boldsymbol{v} + \boldsymbol{v} \cdot \nabla\boldsymbol{v}^{n} - \boldsymbol{v}^{n} \cdot \nabla\boldsymbol{v}^{n}$$

$$= \boldsymbol{v}^{n} \cdot \nabla\boldsymbol{v} + \boldsymbol{v} \cdot \nabla\boldsymbol{v}^{n} - \boldsymbol{v}^{n} \cdot \nabla\boldsymbol{v}^{n}$$

$$= \boldsymbol{v}^{n} \cdot \nabla\boldsymbol{v} + \boldsymbol{v} \cdot \nabla\boldsymbol{v}^{n} - \boldsymbol{v}^{n} \cdot \nabla\boldsymbol{v}^{n}$$

$$= \boldsymbol{v}^{n} \cdot \nabla\boldsymbol{v} + \boldsymbol{v} \cdot \nabla\boldsymbol{v}^{n} - \boldsymbol{v}^{n} \cdot \nabla\boldsymbol{v}^{n}$$

Note that alternative linearizations are considered in different Picard iteration variants where \mathcal{L}_A is taken either as $\mathcal{L}_A \approx \boldsymbol{v}^n \cdot \nabla \boldsymbol{v}$, $\mathcal{L}_A \approx \boldsymbol{v} \cdot \nabla \boldsymbol{v}^n$ or $\mathcal{L}_A \approx \boldsymbol{v}^n \cdot \nabla \boldsymbol{v}^n$.

5. Numerical results

This chapter is dedicated to the presentation of our numerical results obtained with isogeometric finite elements. As aforementioned, the lid-driven cavity flow and flow around cylinder serve as model problems, each discussed in a separate section (5.2, 5.4) in the sequel. Due to the lack of closed form analytical solutions for either benchmark flow scenarios, we first present in section 5.1 our obtained order of convergence for a stationary Stokes flow problem with a closed form analytical solution, before turning the attention to the principal benchmarks.

5.1. Order of convergence of a Stokes flow problem with analytical solution

The considered two-dimensional stokes flow problem consists of finding a velocity field $\mathbf{v} = (v_1, v_2)$ and a pressure p on the square domain $\Omega = (0, 1) \times (0, 1)$ such that

$$-\nu \nabla^{2} \boldsymbol{v} + \nabla p = \boldsymbol{b} \quad \text{in } \Omega,$$

$$\nabla \cdot \boldsymbol{v} = 0 \quad \text{in } \Omega,$$

$$\boldsymbol{v} = \boldsymbol{v}_{D} \quad \text{on } \Gamma_{D},$$
(26)

where the kinematic viscosity is taken as $\nu = 1$. The body force $\mathbf{b} = (b_1, b_2)$ and exact solution $\mathbf{v}^* = (v_1^*, v_2^*, p^*)$ are given as

$$b_1 = 6x + y\cos(xy) + 2\cos(y)\sin(x), b_2 = x\cos(xy) - 2\cos(x)\sin(y),$$
(27)

and

$$v_1^* = \sin(x)\cos(y),$$

$$v_2^* = -\sin(y)\cos(x),$$

$$p^* = 3x^2 + \sin(xy) - 1.239811742000564725943866,$$
(28)

respectively. ² The exact solution for velocity is prescribed as Dirichlet boundary condition on all four sides of Ω , and as far as pressure is concerned, we require: $\int_{\Omega} p \, d\Omega = 0$.

Figure 3 illustrates the L^2 -errors of the velocity and pressure function approximations for different isogeometric discretizations with varied degrees and regularities. The results verify optimal convergence rates for both velocity and pressure. In particular, keeping the degrees fixed, the discretizations with higher regularities are shown to possess the same rate of convergence as their lower regularity counterparts, while remaining much more efficient. As elaborated in section 5.4.1, the efficiency is in terms of the number of degrees of freedom required to gain a certain level of accuracy.

5.2. Lid-driven cavity flow

The classical driven cavity flow benchmark considers a fluid in a square cavity with height H=1. The left, bottom and right walls exhibit no-slip Dirichlet boundary conditions $(\boldsymbol{u}=0)$, while the top "wall" is moved with a constant speed U=1. The volumetric force \mathbf{f} is defined to be 0. A schematic representation of the problem statement is given in Figure

²The exact solution and the corresponding body force term is kindly borrowed from the Matlab based IGA package GeoPDEs.

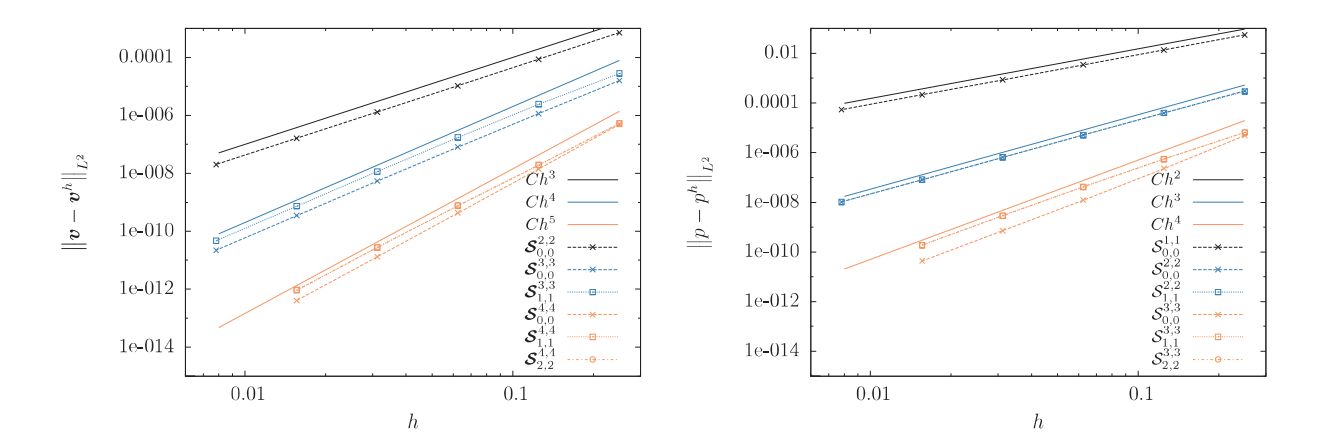


Figure 3: Stokes flow: L^2 -errors of the velocity and pressure approximations obtained with isogeometric discretizations of various degrees and regularities.

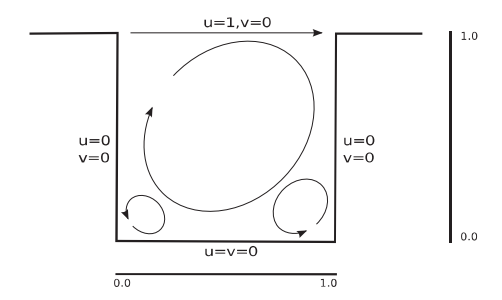


Figure 4: Sketch of lid-driven cavity model.

4. At the upper left and right corners, there is a discontinuity in the velocity boundary conditions producing a singularity in the pressure field at those corners. They can either be considered as part of the upper boundary or as part of the vertical walls. The former case is referred to as the "leaky" cavity rendering the latter "non-leaky". As Dirichlet boundary conditions are imposed everywhere on the boundary ($\Gamma_N = \emptyset$), pressure is in equation (17) only present by its gradient, and thus it is only determined up to an arbitrary constant. For a unique definition of the discrete pressure field, it is usual to either impose its average (e.g. $\int_{\Omega} p \, d\Omega = 0$) or fix its value at one point. We follow the latter approach and fix the value of the discrete pressure field with the value 0 at the lower left corner of the cavity.

Our results, obtained with various B-spline space-based discretizations for three consecutive mesh refinement levels $h \in [1/32, 1/64, 1/128]$ of unstretched meshes, are compared to classical reference results from the literature such as those of Ghia [12] using a second-order upwind finite difference method on a stretched mesh with 192² grid points. Moreover, additional comparisons are done with highly accurate, spectral method-based (Chebyshev Collocation) solutions of Botella [4] that show convergence up to seven digits. Furthermore, whenever comparable data is provided, results of two recently published articles [9, 21], both applying IGA to the cavity flow problem, are addressed. All our computations for cavity flow are performed without taking any stabilization measures for the advection term. As for the Newton iteration, the stopping criterion is considered fulfilled when the euclidean norm of

the residual of equation (17) drops below the bound 10^{-10} .

Using the B-spline space pair $\mathcal{S}_{0,0}^{2,2} \times \mathcal{S}_{0,0}^{1,1}$ for the approximation of the velocity and pressure functions, we present in Figure 5 stream function (ψ) and vorticity (ω) profiles computed for Reynolds (Re) numbers 100, 400 and 1000. Given the circumstance that profiles for ψ and ω

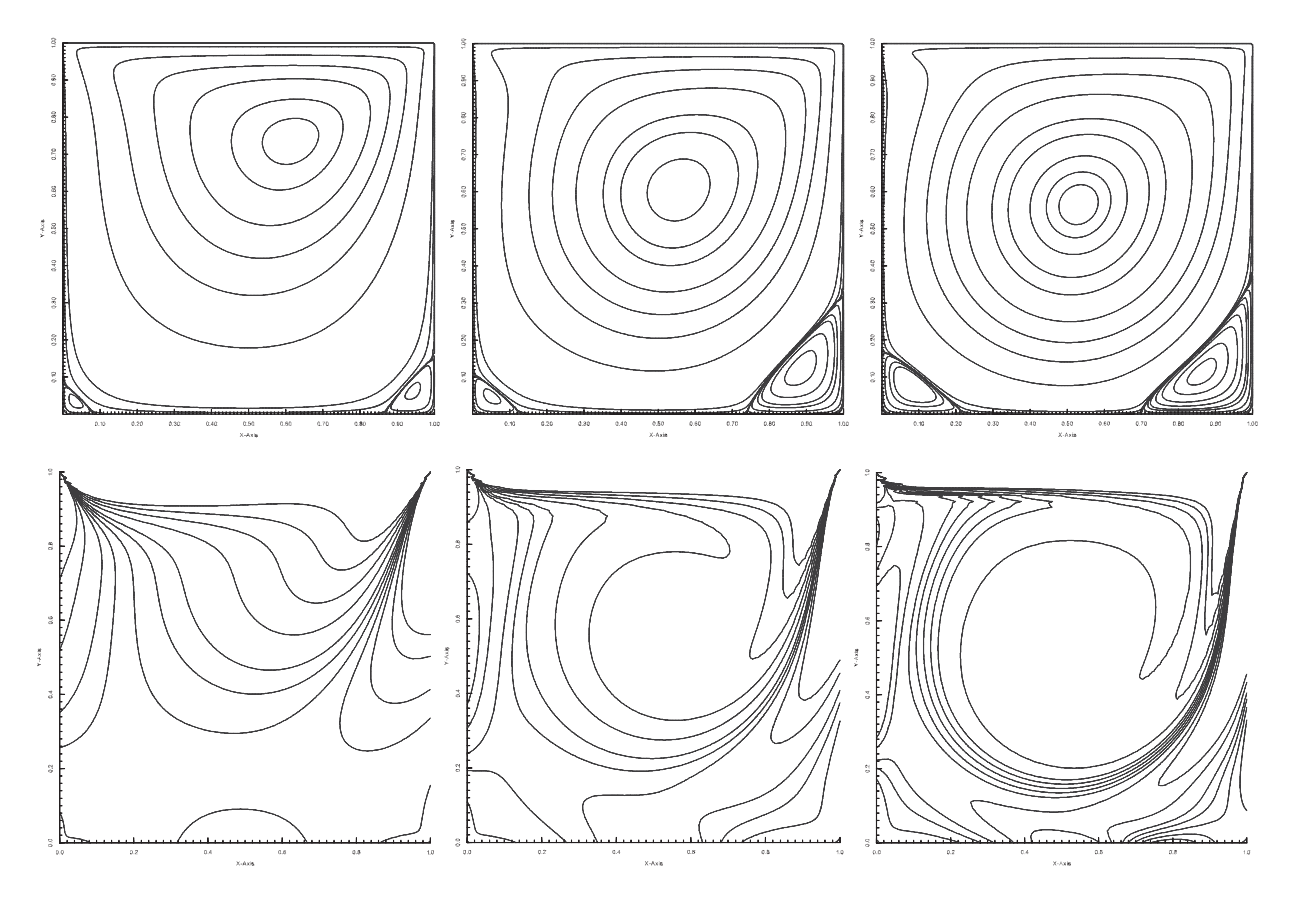


Figure 5: Stream function (top) and vorticity (bottom) profiles for Reynolds 100, 400 and 1000 from left to right. Respective contour ranges for stream function and vorticity: $\psi_{iso} \in [-10^{-10}, 3 \times 10^{-3}], \ \omega_{iso} \in [-5, 3].$ Discretization: $\mathcal{S}_{0,0}^{2,2} \times \mathcal{S}_{0,0}^{1,1}$. h = 1/64 (Refinement level: 6). Number of degrees of freedom: 37507.

are provided by all mentioned references in graphical form only, we conclude the discussion on stream function and vorticity profiles with the note that visually both profiles match the corresponding profiles in the literature very well.

Remark 1. The approach we follow for the computation of the stream function in 2D, is based on solving a Poisson equation for ψ with the scalar 2D vorticity function on the right hand side:

$$-\nabla^2 \psi = \omega$$

$$\omega = \nabla \times \mathbf{v} = \frac{\partial v}{\partial x} - \frac{\partial u}{\partial y}$$
(29)

Equation (29) is easily solvable via FEM/IGA when formulated as a unique boundary value problem in the domain Ω enclosed by the boundary Γ . We set Dirichlet boundary conditions of 0 on the entire boundary when solving for ψ .

In Table 1, stream function and vorticity values at the center of the main vortex are presented for Reynolds numbers 100, 400, and 1000 and compared to the reference values of Ghia, Botella, and the stream function-based Galerkin IGA scheme of [21]. For each Reynolds number we present values for two different Isogeometric discretizations $(\mathcal{S}_{0,0}^{2,2} \times \mathcal{S}_{0,0}^{1,1})$ and $\mathcal{S}_{4,4}^{6,6} \times \mathcal{S}_{4,4}^{5,5}$, and additionally vary for the latter the mesh refinement among three consecutive stages. Note that in Botella's case the flow is reversed, that is, the velocity at the upper boundary is $\boldsymbol{u}=(-1,0)$. However, the flow attributes obtained are mirror-symmetric and comparable to those of older references, such as Ghia's. Botella's results, based on a Chebyshev Collocation method with polynomial degrees as high as 160, are considered highly accurate and motivated the usage of a high degree B-splines space pair such as $\mathcal{S}_{4,4}^{6,6} \times \mathcal{S}_{4,4}^{5,5}$. On a general note, for all Reynolds numbers under consideration, our results are considered converged and in good agreement with the references. Without any exception, both Isogeometric discretizations yield values for the position of the main vortex itself, and stream function and vorticity at the main vortex which are closer to Botella's than Ghia's results. A comparison with the stream function formulation based IGA results of [21] reveals matching positions of the main vortex up to four decimal digits for all Reynolds numbers, discretizations, and mesh refinement levels. Our stream function values match [21] very well, but are shown for Re 1000 to be minimally closer to Botella's results for both discretizations and all mesh refinement levels. Coming up next, we depict our approximations of the u- and v-velocity components along vertical and horizontal lines through the geometric center of the cavity, respectively. The corresponding profiles obtained with a $\mathcal{S}_{0,0}^{2,2} \times \mathcal{S}_{0,0}^{1,1}$ discretization for $h \in [1/32, 1/64, 1/128]$ are presented graphically alongside those of Ghia in Figure 6. Except for one irregularity with respect to the v-velocity component (see Fig. 6) computations in the Re 400 case, the converged profiles follow the reference data of Ghia and reflect the profiles presented in the isogeometric references [9, 21].

The extrema of the velocity components along horizontal and vertical lines through the geometric center of the cavity are listed in Table 2 and compared to both isogeometric and the classical references. As can be seen from the tabulated data, the results of the isogeometric Taylor—Hood discretization are closest to those of Botella obtained with a spectral method.

Taylor-Hood discretization are closest to those of Botella obtained with a spectral method. In addition to the presented results regarding the $\mathcal{S}_{0,0}^{2,2} \times \mathcal{S}_{0,0}^{1,1}$ discretization, we deliver additional ones associated to both an approximation space pair with higher regularity $\mathcal{S}_{4,4}^{6,6} \times \mathcal{S}_{4,4}^{5,5}$ (\mathcal{C}^4) and a reversed flow direction (u = (-1,0)), such as the setup used by Botella. A graphical representation of converged velocity component and vorticity data approximated in the above described \mathcal{C}^4 space pair, exhibiting excellent agreement with the ones stemming from Botella's spectral method, is illustrated in Figure 7.

5.3. Regularized driven cavity flow

In the regularized lid-driven cavity flow scenario as described in [5], the flow domain is a unit square exhibiting no-slip Dirichlet boundary conditions at the vertical and lower horizontal boundaries. In order to avoid the pressure singularities in the upper left and right domain corners involved with the regular lid-driven cavity flow scenario, the regularized lid-driven cavity flow problem defines the following velocity profile on the top boundary

$$\mathbf{u}_{lid} = [-16x^2(1-x)^2, 0]. \tag{30}$$

In addition to the study of local quantities, it is reasonable to extend the analysis to global quantities. Towards this end, we fix the value of the discrete pressure field at the lower

Re	Scheme	x	y	ψ	ω	N_{el}	h	N_{dof}	$N_{dof(vel.\ +\ pres.)}$	Grid points
100	$m{\mathcal{S}}_{0,0}^{2,2} imes m{\mathcal{S}}_{0,0}^{1,1}$	0.6150	0.7350	-0.103524	3.15526	32^{2}	1/32	9539	(8450+1089)	65^{2}
	$\mathcal{S}_{0,0}^{2,2} imes \mathcal{S}_{0,0}^{1,1}$	0.6150	0.7350	-0.103517	3.15350	64^{2}	1/64	37507	(33282+4225)	129^{2}
	$\mathcal{S}_{0.0}^{2,2} imes \mathcal{S}_{0.0}^{1,1}$	0.6150	0.7350	-0.103516	3.15377	128^{2}	1/128	148739	(132098+16641)	257^{2}
	$oldsymbol{\mathcal{S}}^{6,6}_{4,4} imes oldsymbol{\mathcal{S}}^{5,5}_{4,4}$	0.6150	0.7350	-0.103516	3.15382	32^{2}	1/32	10891	(9522+1369)	69^{2}
	$\mathcal{S}_{4 4}^{6,6} imes\mathcal{S}_{4 4}^{5,5}$	0.6150	0.7350	-0.103516	3.15383	64^{2}	1/64	40139	(35378+4761)	133^{2}
	$\mathcal{S}_{4,4}^{ar{6},ar{6}} imes \mathcal{S}_{4,4}^{ar{5},ar{5}}$	0.6150	0.7350	-0.103516	3.15383	128^{2}	1/128	153931	(136242+17689)	261^{2}
	Ghia [12]	0.6172	0.7344	-0.103423	3.16646		1/128			129^{2}
	[21]	0.6150	0.7350	-0.103518		256^{2}	1/256	66564		258^{2}
400	$\mathcal{S}^{2,2}_{0,0} imes \mathcal{S}^{1,1}_{0,0}$	0.5550	0.6050	-0.114019	2.29555	32^{2}	1/32	9539	(8450+1089)	65^{2}
	$\mathcal{S}_{0,0}^{2,2} imes \mathcal{S}_{0,0}^{1,1}$	0.5550	0.6050	-0.113996	2.29470	64^{2}	1/64	37507	(33282+4225)	129^{2}
	$\mathcal{S}_{0.0}^{2,2} imes \mathcal{S}_{0.0}^{1,1}$	0.5550	0.6050	-0.113989	2.29449	128^{2}	1/128	148739	(132098+16641)	257^{2}
	$\mathcal{S}^{6,6}_{4 4} imes\mathcal{S}^{5,5}_{4 4}$	0.5550	0.6050	-0.113985	2.29448	32^{2}	1/32	10891	(9522+1369)	69^{2}
	$\mathcal{S}_{4,4}^{\ddot{6},\ddot{6}} imes \mathcal{S}_{4,4}^{\ddot{5},\ddot{5}} \ \mathcal{S}_{4,4}^{6,6} imes \mathcal{S}_{4,4}^{5,5}$	0.5550	0.6050	-0.113988	2.29448	64^{2}	1/64	40139	(35378+4761)	133^{2}
	$\mathcal{S}^{6,6}_{4,4} imes\mathcal{S}^{5,5}_{4,4}$	0.5550	0.6050	-0.113988	2.29448	128^{2}	1/128	153931	(136242+17689)	261^{2}
	Ghia $[12]$	0.5547	0.6055	-0.113909	2.29469		1/256			257^{2}
	[21]	0.5550	0.6050	-0.114031		256^{2}	1/256	66564		258^{2}
1000	$m{\mathcal{S}}_{0,0}^{2,2} imes m{\mathcal{S}}_{0,0}^{1,1}$	0.5300	0.5650	-0.1189603	2.070030	32^{2}	1/32	9539	(8450+1089)	65^{2}
	$\mathcal{S}_{0.0}^{2,2} imes \mathcal{S}_{0.0}^{1,1}$	0.5300	0.5650	-0.1189511	2.067930	64^{2}	1/64	37507	(33282+4225)	129^{2}
	$\mathcal{S}_{0.0}^{2,2} imes \mathcal{S}_{0.0}^{1,1}$	0.5300	0.5650	-0.1189400	2.067790	128^{2}	1/128	148739	(132098+16641)	257^{2}
	$\mathcal{S}_{4.4}^{6,6} imes \mathcal{S}_{4.4}^{5,5}$	0.5300	0.5650	-0.1189165	2.067510	32^{2}	1/32	10891	(9522+1369)	69^{2}
	$\mathcal{S}_{4.4}^{\scriptscriptstyle 5,5} imes\mathcal{S}_{4.4}^{\scriptscriptstyle 5,5}$	0.5300	0.5650	-0.1189341	2.067710	64^{2}	1/64	40139	(35378+4761)	133^{2}
	$\mathcal{S}_{4,4}^{6,6} imes\mathcal{S}_{4,4}^{5,5}$	0.5300	0.5650	-0.1189360	2.067730	128^{2}	1/128	153931	(136242+17689)	261^{2}
	Botella [4]	0.5308	0.5652	-0.1189249	2.067396		1/48			N = 48
	Botella [4]	0.5308	0.5652	-0.1189366	2.067750		1/96			N = 96
	Botella [4]	0.5308	0.5652	-0.1189366	2.067753		1/160			N = 160
	Ghia [12]	0.5313	0.5625	-0.1179290	2.049680	0	1/128			129^2
	[21]	0.5300	0.5650	-0.1185110		256^{2}	1/256	66564		258^{2}

Table 1: Location, stream function and vorticity of the primary vortex for Re 100, 400 and 1000. N is used to characterize the $N+1\times N+1$ Gauss-Lobatto grid used in the Chebyshev Collocation method utilized by Botella. In the case of the Isogeometric discretizations we carried our computations upon, the element meshes are uniformly spaced and "grid points" refers to the number of basis functions (degrees of freedom) of the respective discrete approximation space for one velocity component. N_{dof} and N_{el} represent the number of degrees of freedom and the number of elements, respectively.

Re	Center line	Property	$S_{0.0}^{2.2} \times S_{0.0}^{1.1}(h = 1/128)$	Botella [4]	Ghia [12]	[9] $(h = 1/128)$	[21] $(h = 1/256, p = 2)$
100	Vertical	u_{min}	-0.21404	-0.21404	-0.21090	-0.21414	-0.21402
	(x = 0.5)	y-coord	0.4578	0.4581	0.4531		0.4600
	Horizontal	v_{min}	-0.25380	-0.25380	-0.24533	-0.25387	-0.25371
	(y = 0.5)	x-coord	0.8112	0.8104	0.8047		0.8100
		v_{max}	0.17957	0.17957	0.17527	0.17966	0.17953
		x-coord	0.2369	0.2370	0.2344		0.2350
400	Vertical	u_{min}	-0.32872		-0.32726	-0.32989	-0.32880
	(x = 0.5)	y-coord	0.2811		0.2813		0.2800
	Horizontal	v_{min}	-0.45402		-0.44993	-0.45470	-0.45386
	(y = 0.5)	x-coord	0.8635		0.8594		0.8600
		v_{max}	0.30383		0.30203	0.30471	0.30393
		x-coord	0.2249		0.2266		0.2250
1000	Vertical	u_{min}	-0.38857	-0.38853	-0.38289	-0.39021	-0.38754
	(x = 0.5)	y-coord	0.1727	0.1717	0.1719		0.1700
	Horizontal	v_{min}	-0.52692	-0.52707	-0.51550	-0.52884	-0.52582
	(y = 0.5)	x-coord	0.9076	0.9092	0.9063		0.9100
	,	v_{max}	0.37694	0.37694	0.37095	0.37856	0.37572
		x-coord	0.1566	0.1578	0.1563		0.1600

Table 2: Extrema of the velocity components w.r.t vertical and horizontal lines through the geometric center of the cavity for Re 100, 400 and 1000.

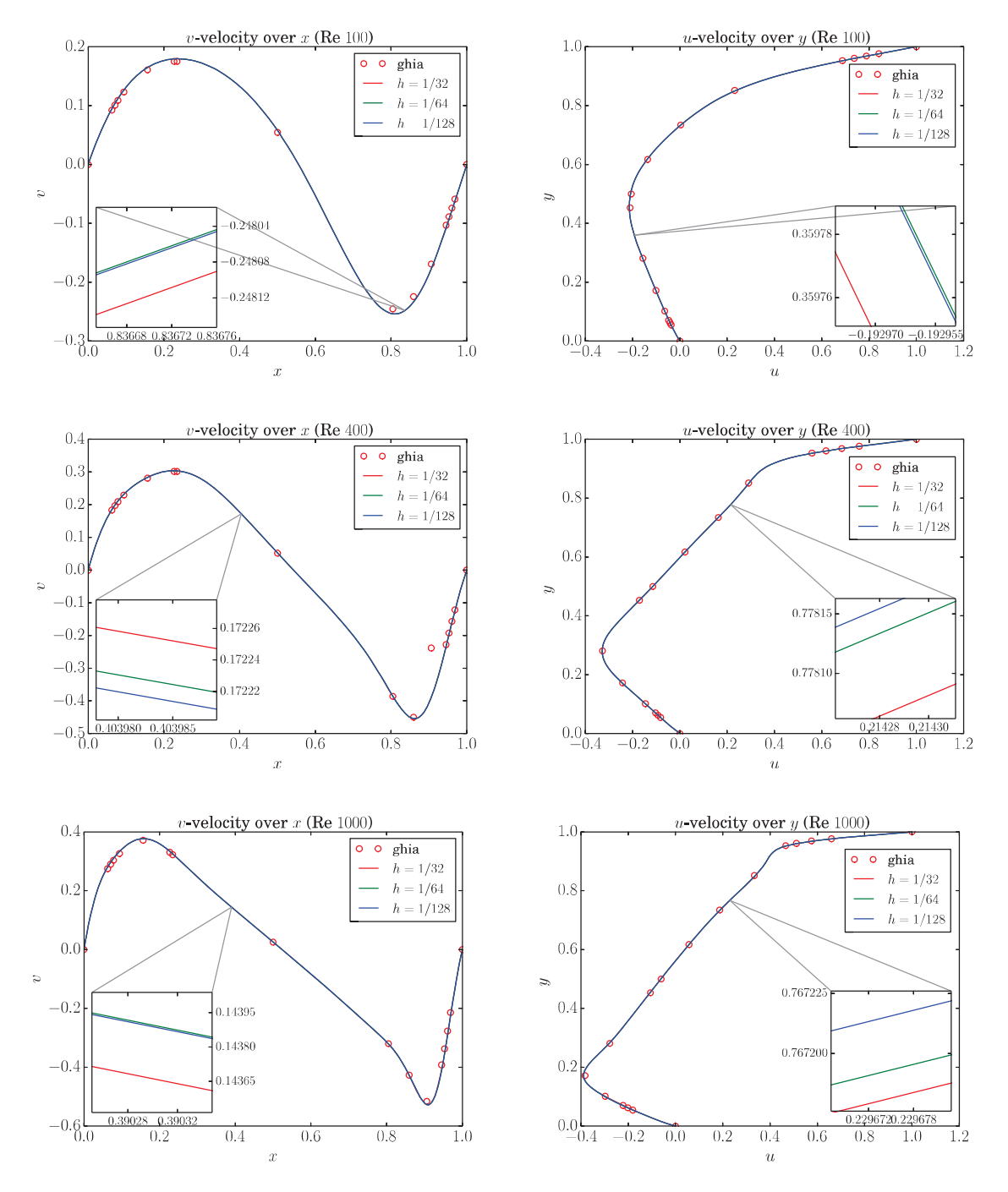


Figure 6: Profiles of v- and u-velocity components over horizontal and vertical lines through geometric center of the cavity for Re 100, 400 and 1000. Discretization: $\mathcal{S}_{0,0}^{2,2} \times \mathcal{S}_{0,0}^{1,1}$; See Table 1 for the number of degrees of freedom.

left domain node with p=0, and compute the global quantities KINETIC ENERGY (E) and ENSTROPHY (Z)

$$E = \frac{1}{2} \int_{\Omega} \|\mathbf{u}\|^2 dx, \quad Z = \frac{1}{2} \int_{\Omega} \omega^2 dx, \tag{31}$$

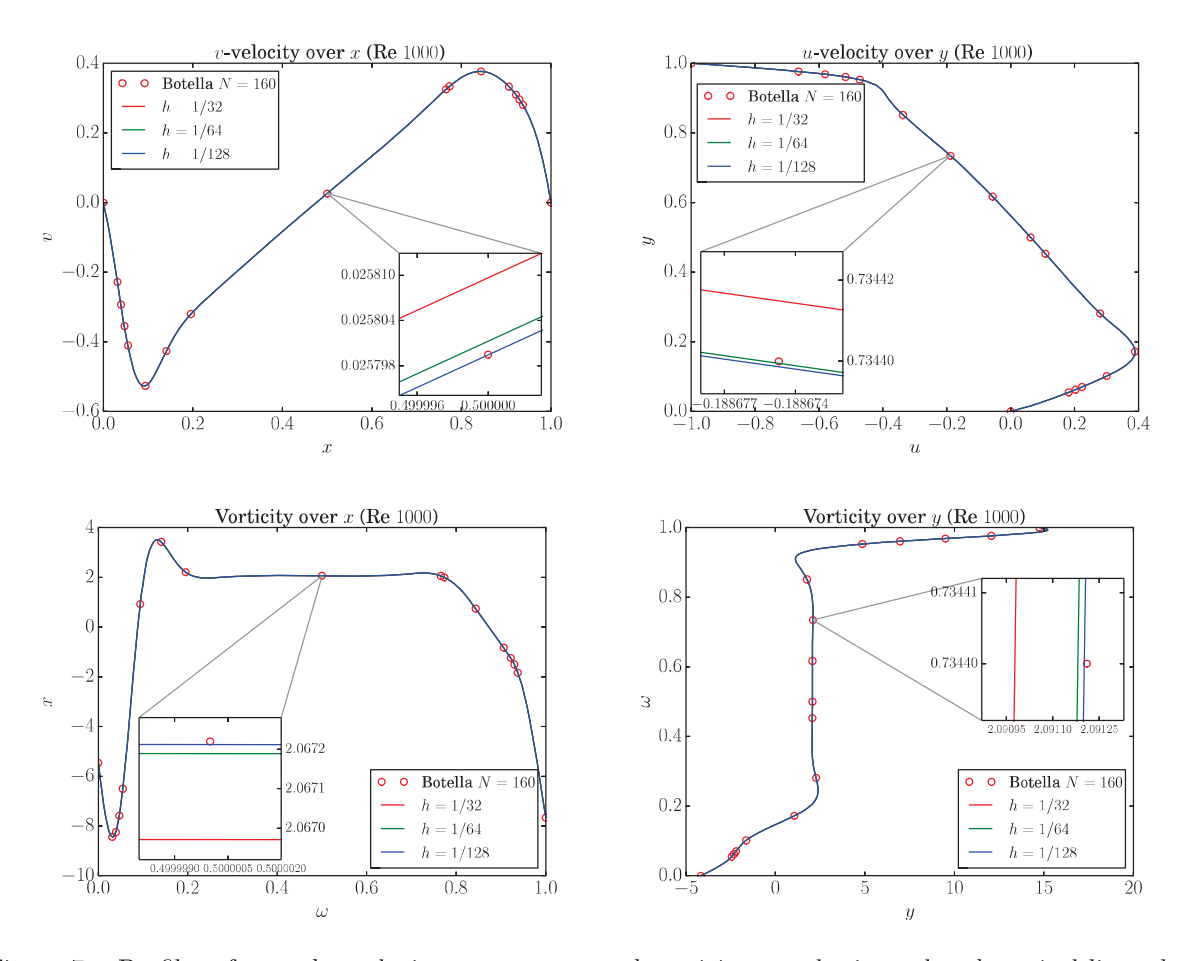


Figure 7: Profiles of v- and u-velocity components and vorticity over horizontal and vertical lines through geometric center of the cavity for Re 1000. Discretization: $\mathcal{S}_{4,4}^{6,6} \times \mathcal{S}_{4,4}^{5,5}$; See Table 1 for the number of degrees of freedom.

where $\omega = \frac{\partial v}{\partial x} - \frac{\partial u}{\partial y}$ denotes the scalar vorticity in 2D. In Table 3 we compare our results for Reynolds number 1000, computed on unstretched meshes, to the results of Bruneau [5] using finite differences and a 3Q_2P_1 finite element discretization, published in [17]. All three isogeometric finite element pairs in charge produce very satisfying results for kinetic energy and enstrophy obviously well integrating with references. Selecting the isogeometric finite element pair with the lowest degree $\mathcal{S}_{0,0}^{2,2} \times \mathcal{S}_{0,0}^{1,1}$, we compare in Table 4 the approximated kinetic energy for three mesh refinement levels with data [17] obtained from three different finite element discretizations, namely⁴, \tilde{Q}_1Q_0 , Q_2P_1 , and⁵ W-LSFE Q_2 , all available in the FEATFLOW⁶ package. As can be deduced from the tabulated data, our results are characterized by both a high accuracy and a satisfactory convergence for all considered Reynolds numbers.

³Velocity: Biquadratic, continuous; Pressure: Linear (value and two partial derivatives), discontinuous

⁴Velocity: Bilinear, rotated; Pressure: Constant.

⁵Biquadratic Least-Square finite elements.

⁶www.featflow.de.

Scheme	Kinetic Energy	Enstrophy	$N_{\rm el}$	h	N_{dof}	$N_{dof(vel. + pres.)}$	Grid points
$m{\mathcal{S}}_{0,0}^{2,2} imes \mathcal{S}_{0,0}^{1,1}$	0.022909	4.80747	32^{2}	1/32	9539	(8450+1089)	65^{2}
0,0	0.022778	4.82950	64^{2}	1/64	37507	(33282+4225)	129^{2}
	0.022767	4.83041	128^{2}	1/128	148739	(132098+16641)	257^{2}
	0.022767	4.83043	256^{2}	1/256	592387	(526338+66049)	513^{2}
$m{\mathcal{S}}_{0,0}^{3,3} imes \mathcal{S}_{0,0}^{2,2}$	0.022905	4.81717	16^{2}	1/16	5891	(4802+1089)	49^{2}
, ,	0.022773	4.83079	32^{2}	1/32	23043	(18818+4225)	97^{2}
	0.022767	4.83047	64^{2}	1/64	91139	(74498+16641)	193^{2}
	0.022767	4.83042	128^{2}	1/128	362499	(296450 + 66049)	385^{2}
$\mathcal{S}_{1.1}^{3,3} imes \mathcal{S}_{1.1}^{2,2}$	0.022777	4.82954	32^{2}	1/32	9868	(8712+1156)	66^{2}
-,,-	0.022767	4.83048	64^{2}	1/64	38156	(33800+4356)	130^{2}
	0.022767	4.83046	128^{2}	1/128	150028	(133128+16900)	258^{2}
Ref. [5] (Bruneau)	0.021564	4.6458					64^{2}
	0.022315	4.7711					128^{2}
	0.022542	4.8123					256^{2}
	0.022607	4.8243					512^{2}
Ref. [17] $(Q_2P_1 \text{ FE})$	0.022778	4.82954	64^{2}	1/64			
	0.022768	4.83040	128^{2}	1/128			
	0.022766	4.83050	256^{2}	1/256			

Table 3: Kinetic energy and enstrophy of the regularized cavity flow for Reynolds 1000. In the case of Isogeometric discretizations, "grid points" refers to the number of basis functions (degrees of freedom) of the respective discrete approximation space for one velocity component.

Re	h	$m{\mathcal{S}}_{0,0}^{2,2} imes m{\mathcal{S}}_{0,0}^{1,1}$	\tilde{Q}_1Q_0 FE	Q_2P_1 FE	W-LSFE Q_2 [17]
1	1/64	1.862439E-02	1.860621E-02	1.862439E-02	1.862353E-02
	1/128	1.862438E-02	1.861982E- 02	1.862438E-02	1.862432E-02
	1/256	1.862438E-02	1.862324E-02	1.862438E-02	1.862438E-02
400	1/64	2.131703E-02	2.148649E-02	2.131707E-02	2.133053E-02
	1/128	2.131547E-02	2.136484E-02	2.131547E-02	2.131581E-02
	1/256	2.131537E-02	2.132812E-02	2.131529E-02	2.131537E-02
1000	1/64	2.277788E-02	2.409799E-02	2.277778E-02	2.552796E-02
	1/128	2.276761E-02	2.305179E-02	2.276761E-02	2.287704E-02
	1/256	2.276692E-02	2.282649E-02	2.276582E-02	2.277389E-02

Table 4: Convergence of approximated kinetic energy for the regularized cavity flow problem.

5.4. Flow around cylinder

Flow around an obstacle in a channel is a prominent benchmark model for the assessment of flow affiliated attributes, produced by a numerical technique in charge with the analysis. Following the lines of [10, 11, 16, 19], we choose as flow scenarios a steady Re 20 and a transient Re 100 2D channel flow the details of which are presented in sections 5.4.1 and 5.4.2, respectively. The underlying geometry for both cases is depicted in Figure 8 and is defined as a pipe where a circular cylinder of radius r = 0.05 has been cut out, that is, $\Omega = (0, 2.2) \times (0, 0.41) \setminus B_r(0.2, 0.2)^7$. The cylinder is centered around (x, y) = (0.2, 0.2).

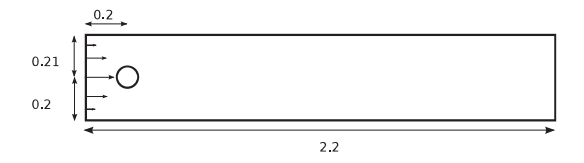


Figure 8: Computational domain for flow around cylinder.

5.4.1. DFG benchmark 2D-1

In DFG BENCHMARK 2D-1 the fluid density and kinematic viscosity are taken as $\rho=1$ and $\nu=0.001$. We require no-slip boundary conditions for the lower and upper walls $\Gamma_1=(0,2.2)\times\{0\}$ and $\Gamma_3=(0,2.2)\times\{0.41\}$, as well as for the boundary $S=\partial B_r(0.2,0.2)$: $u_{|\Gamma_1}=u_{|\Gamma_3}=u_{|S}=0$. On the left edge $\Gamma_4=\{0\}\times(0,0.41)$, a parabolic inflow profile is prescribed, $u(0,y)=\left(\frac{4Uy(0.41-y)}{0.41^2},0\right)$, with a maximum velocity U=0.3. On the right edge $\Gamma_2=\{2.2\}\times(0,0.41)$, "do-nothing" boundary conditions, $-pn+\nu(n\cdot\nabla)v=0$, define the outflow, with n denoting the outer normal vector. For a maximum velocity of U=0.3, the parabolic profile results in a mean velocity $\bar{U}=\frac{2}{3}\cdot0.3=0.2$. The flow configurations characteristic length $D=2\cdot0.05=0.1$ is the diameter of the object perpendicular to the flow direction. This particular problem configuration yields Reynolds number $\mathrm{Re}=\frac{\bar{U}D}{\nu}=\frac{0.2\cdot0.1}{0.001}=20$ for which the flow is considered stationary.

Following the above setup for Re = 20, we present the results of the application of Isogeometric Analysis, with particular emphasis on the approximated drag and lift values related to the entire obstacle boundary.

With S dubbing the surface of the obstacle, \mathbf{n}_S its inward pointing unit normal vector w.r.t. the computational domain Ω , tangent vector $\boldsymbol{\tau} := (n_y, -n_x)^T$ and $\mathbf{u}_{\tau} := \mathbf{u} \cdot \boldsymbol{\tau}$, the drag and lift forces are given by

$$F_{D} = \int_{S} \left(\rho \nu \frac{\partial \mathbf{u}_{\tau}}{\partial \mathbf{n}_{S}} n_{y} - p n_{x} \right) ds, \quad F_{L} = -\int_{S} \left(\rho \nu \frac{\partial \mathbf{u}_{\tau}}{\partial \mathbf{n}_{S}} n_{x} + p n_{y} \right) ds$$

$$C_{D} = \frac{2}{\rho \bar{U}^{2} D} F_{D}, \quad C_{L} = \frac{2}{\rho \bar{U}^{2} D} F_{L},$$
(32)

where C_D and C_L are the drag and lift coefficients, and u and p represent velocity and pressure, respectively [15, 19]. We follow, however, the alternative approach of [15, 23] and

⁷The presented measures for the domain definition are in meters.

evaluate a volume integral for the approximations of the drag and lift coefficients. Given filter functions

$$\mathbf{v}_{d|S} = (1,0)^T, \mathbf{v}_{d|\bar{\Omega}-S} = \mathbf{0}$$
 $\mathbf{v}_{l|S} = (0,1)^T, \mathbf{v}_{l|\bar{\Omega}-S} = \mathbf{0},$ (33)

the corresponding volume integral expressions read

$$C_{D} = -\frac{2}{\rho \bar{U}^{2} D} \left[(\nu \nabla \boldsymbol{u}, \nabla \boldsymbol{v_{d}}) - (p, \nabla \cdot \boldsymbol{v_{d}}) \right]$$

$$C_{L} = -\frac{2}{\rho \bar{U}^{2} D} \left[(\nu \nabla \boldsymbol{u}, \nabla \boldsymbol{v_{l}}) - (p, \nabla \cdot \boldsymbol{v_{l}}) \right],$$
(34)

with (\cdot,\cdot) denoting the $L^2(\Omega)$ inner product. Note that in the discrete setting, we use the respective interpolants of the discontinuous filter functions \mathbf{v}_d and \mathbf{v}_l .

We model the computational domain as a multi-patch NURBS mesh (see Fig. 9), due to the fact that the parametric space of a multi-variate NURBS patch exhibits a tensor product structure, and thus is not mappable to any other topology than a cube in the respective N-dimensional space. However, the multi-patch setup yields a perfect mathematical representation of the circular boundary and in particular avoids its approximation with straight line segments. Note that each quarter of the "obstacle circle" can be modeled exactly with a NURBS curve of degree 2 and just 3 control points. Since the ability to exactly represent conical sections is restricted to rational B-splines only, a NURBS mesh comes in handy for the modeling of the computational domain. In order to impose the parabolic inflow condition,

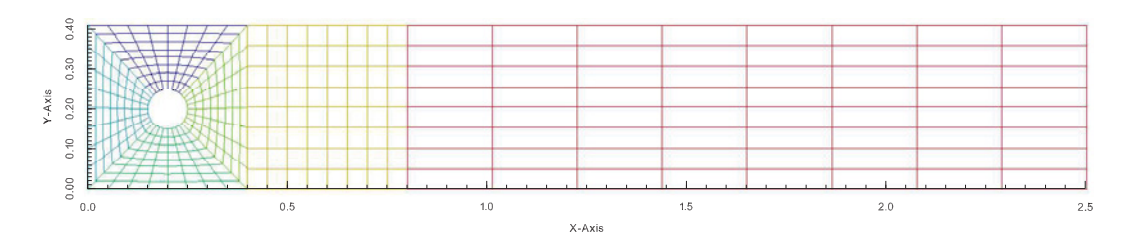


Figure 9: Multi-patch NURBS mesh for flow around cylinder at refinement level 3. Each uniquely colored initial 1×1 element patch has been refined three times, giving rise to 8×8 elements in each patch, eventually.

we perform a finite element L^2 -projection

$$\int_{\Gamma_4} (f - P_h f) w \, d\Gamma_4 = 0, \quad \forall w \in \mathcal{W}_h$$
(35)

of the inflow profile f on the control points associated with the left boundary (Γ_4) in Fig. 9, whereby \mathcal{W}_h denotes a suitable discrete space of weighting/test functions.

For the approximation of drag, lift, and pressure drop we use two different isogeometric discretizations, namely, $\mathcal{S}_{0,0}^{3,3} \times \mathcal{S}_{0,0}^{2,2}$ and $\mathcal{S}_{1,1}^{3,3} \times \mathcal{S}_{1,1}^{2,2}$, and compare their results for different mesh refinement levels with a reference solution computed with high order spectral methods [16]. The choice of these two isogeometric discretizations is explained by the fact that we require the discrete pressure approximation space to have the same degrees and regularities as the geometry. Since modeling one quarter of the obstacle circle requires a NURBS curve of

at least degree 2, the degrees of the discrete pressure approximation space reflect this setting. The degrees and regularities of the discrete velocity approximation space eventually follow from the constraints defined by Taylor–Hood elements (see e.g. [6]). In fact, given an initial discrete pressure space, we use k-refinement [7] followed by knot insertion to setup a desired Taylor–Hood space of higher degree and possibly lower regularity.

We refer to table 5 for a compilation of the approximated forces for different mesh refinement levels. Our results exhibit high accuracy on the highest mesh refinement level (L8), since a comparison with the reference data reveals 4, 6, and 7 matching decimal digits for drag, lift, and pressure drop, respectively. Moreover, starting with mesh refinement level 6,

Scheme	C_D	C_L	Δp	$N_{ m dof}$	N_{el}	Level
$m{\mathcal{S}}_{0,0}^{3,3} imes \mathcal{S}_{0,0}^{2,2}$	5.645768	0.0067650	0.11675114	8832	384	L3
$oldsymbol{\mathcal{S}}_{0,0}^{3,3} imes \mathcal{S}_{0,0}^{2,2}$	5.594618	0.0095045	0.11733243	34560	1536	L4
$oldsymbol{\mathcal{S}}_{0,0}^{3,3} imes \mathcal{S}_{0,0}^{2,2}$	5.582119	0.0104074	0.11749107	136704	6144	L5
$oldsymbol{\mathcal{S}}_{0,0}^{3,3} imes \mathcal{S}_{0,0}^{2,2}$	5.579918	0.0105860	0.11751658	543744	24576	L6
$oldsymbol{\mathcal{S}}_{0,0}^{3,3} imes \mathcal{S}_{0,0}^{2,2}$	5.579588	0.0106143	0.11751977	2168832	98304	L7
$oldsymbol{\mathcal{S}}^{3,3}_{0,0} imes \mathcal{S}^{2,2}_{0,0}$	5.579543	0.0106183	0.11752012	8663040	393216	L8
$m{\mathcal{S}}_{1,1}^{3,3} imes \mathcal{S}_{1,1}^{2,2}$	5.647333	0.0066836	0.11633509	4212	384	L3
$oldsymbol{\mathcal{S}}_{1,1}^{\hat{3},\hat{3}} imes \mathcal{S}_{1,1}^{\hat{2},\hat{2}}$	5.594742	0.0095065	0.11723232	15300	1536	L4
$m{\mathcal{S}}_{1,1}^{\overset{1}{3},\overset{1}{3}} imes \mathcal{S}_{1,1}^{\overset{1}{2},\overset{1}{2}}$	5.582148	0.0104082	0.11749043	58212	6144	L5
$m{\mathcal{S}}_{1,1}^{3,3} imes \mathcal{S}_{1,1}^{2,2}$	5.579918	0.0105861	0.11751770	226980	24576	L6
$m{\mathcal{S}}_{1,1}^{\overset{1}{3},\overset{1}{3}} imes \mathcal{S}_{1,1}^{\overset{1}{2},\overset{1}{2}}$	5.579588	0.0106143	0.11751993	896292	98304	L7
$oldsymbol{\mathcal{S}}_{1,1}^{3,3} imes \mathcal{S}_{1,1}^{2,2}$	5.579543	0.0106183	0.11752014	3562020	393216	L8
Ref. [11, 16]	5.57953523384	0.010618948146	0.11752016697			

Table 5: Approximation results for drag, lift and pressure drop (Δp) .

the approximated drag and lift coefficients of both isogeometric discretizations are, except for one irregularity, identical with respect to the displayed number of decimal digits. This result is remarkable and advocates the usage of the discretization with higher continuity, since the number of degrees of freedoms it requires to reach the same accuracy on refinement level 7 is approximately 42% of its \mathcal{C}^0 counterpart. The development of this "gain" is illustrated in Figure 10 for mesh refinement levels one to eight. Comparing the presented \mathcal{C}^0 — and \mathcal{C}^1 —based

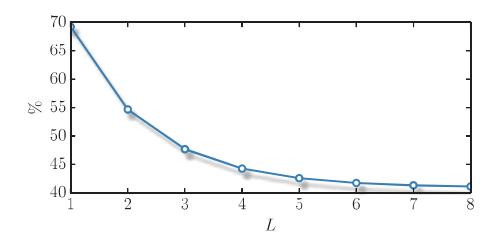


Figure 10: Percentage ratio (DOFs($\mathcal{S}_{1,1}^{3,3} \times \mathcal{S}_{1,1}^{2,2}, L$)/DOFs($\mathcal{S}_{0,0}^{3,3} \times \mathcal{S}_{0,0}^{2,2}, L$) × 100) of the number of degrees of freedom of the \mathcal{C}^1 discretization and the \mathcal{C}^0 discretization for each mesh refinement level L of the flow around cylinder mesh. Table 5 lists the number of degrees of freedom for each L.

isogeometric discretizations, one observes in the former case an increased amount of degrees of

freedom on the same number of elements. This is due to the fact that the discretization with the lower continuity exhibits an increased internal knot multiplicity which in turn implies a larger number of basis functions. This leads on mesh refinement levels ≥ 1 to numbers of degrees of freedom which are not well comparable between the two IGA-based discretizations. However, a linear interpolation of the the drag and lift percent errors, as depicted in Figure 11, bears testimony to the accuracy-wise superiority of the high continuity \mathcal{C}^1 approach. The

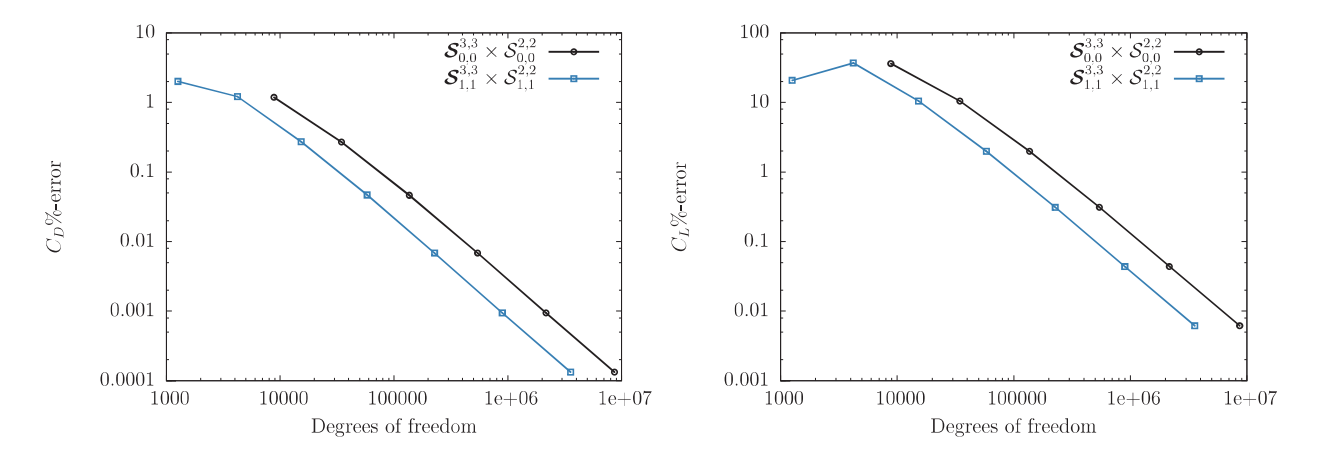


Figure 11: Sectional view of drag and lift percent errors. Discretizations: $\mathcal{S}_{0,0}^{3,3} \times \mathcal{S}_{0,0}^{2,2}$; $\mathcal{S}_{1,1}^{3,3} \times \mathcal{S}_{1,1}^{2,2}$.

semantics of superiority is in terms of gained accuracy with respect to the number of degrees of freedom invested.

Remark 2. We point out that, regardless of the regularity, the support of univariate B-spline and NURBS basis functions of degree p is always p+1 knot spans. In 1D, the number of functions that any given function shares support with (including itself) is 2p+1, and the maximum bandwidth of a stiffness matrix produced with IGA in a Galerkin framework, is always 2p+1 regardless of the smoothness of the basis functions (C^0 or C^{p-1} continuous).

Generally, it should be noted that the solutions we obtained with the $C^{>0}$ approaches still reduce to C^0 at patch boundaries. There exist means to overcome this deficiency [7], none of which have been considered in this study, though. Besides, for all simulations performed, we utilized standard quadrature rules (#cub.pts = p + 1), certainly not the most efficient rules at Isogeometric Analysis' disposal. Finally, for the nonlinear iteration the same stopping criterion as in the lid-driven cavity case is used, that is, it is halted as soon as the euclidean norm of the residual of equation (17) is below 10^{-10} .

5.4.2. DFG benchmark 2D-2

In the following we turn our attention to the DFG BENCHMARK 2D-2 [10, 19] defining an unsteady configuration for the flow around cylinder scenario on the same computational domain as in the DFG BENCHMARK 2D-1 case. The setup aims to simulate the time-periodic behavior of a fluid in a 2D pipe with a circular obstacle. The attention is turned in particular to the resulting drag, lift, and pressure drop profiles which are shown to have an oscillating and periodic structure. These profiles are analyzed with respect to their frequency, amplitude, minimum, maximum, and mean values.

In this benchmark, the maximum velocity of the parabolic inflow profile amounts to U=1.5, yielding $\text{Re} = \frac{\bar{U}D}{\nu} = \frac{\frac{2}{3} \cdot \frac{3}{2} \cdot 0.1}{0.001} = 100$. In order to obtain a time profile for the drag, lift, and pressure drop coefficients, we use again the NURBS mesh shown in Figure 9 and apply Isogeometric Analysis to the unsteady incompressible Navier–Stokes equations (21), using the Taylor–Hood B-spline spaces $\hat{Q}_h^{TH} = \mathcal{S}_{0,0}^{2,2}$ and $\hat{\mathbf{V}}_h^{TH} = \mathcal{S}_{0,0}^{3,3}$ for pressure and velocity, respectively. Treating Eq. (21) as is, i.e. without the application of any operator splitting techniques, corresponds to solving in a fully coupled manner since we solve for all unknown functions simultaneously.

For the time discretization, the single step θ -scheme with $\theta = 0.5$ is used, leading to the 2nd order accurate implicit Crank–Nicolson scheme [22]. Together with the space discretization, the following nonlinear block system has to be solved in every time step

$$\begin{pmatrix} \frac{1}{\Delta t} \mathbf{M} + \theta (\mathbf{D} + \mathbf{C}(v^{n+1})) & \mathbf{G} \\ \mathbf{G}^{T} & \mathbf{0} \end{pmatrix} \begin{pmatrix} \mathbf{v}^{n+1} \\ \mathbf{p}^{n+1} \end{pmatrix} = \begin{pmatrix} \frac{1}{\Delta t} \mathbf{M} - (1-\theta)(\mathbf{D} + \mathbf{C}(v^{n})) & \mathbf{0} \\ \mathbf{0} & \mathbf{0} \end{pmatrix} \begin{pmatrix} \mathbf{v}^{n} \\ \mathbf{p}^{n} \end{pmatrix} + \theta \mathbf{f}^{n+1} + (1-\theta)\mathbf{f}^{n}.$$
(36)

In the above system, $\mathbf{M}, \mathbf{D}, \mathbf{C}, \mathbf{G}$, and $\mathbf{G}^{\mathbf{T}}$ denote the mass, diffusion, advection, gradient, and divergence matrices, respectively. The body forces are discretized into \mathbf{f} . As far as the treatment of nonlinearity is concerned, for every time step, the nonlinear iteration is advanced until the nonlinear residual of equation (36) is reduced to 10^{-3} of its initial value.

For all mesh levels we performed an intermediate computation with a very coarse time step ($\Delta t = 1/10$) for a total time of 35 simulation seconds. This yielded a profile which we took as an initial solution for the final computation with a finer time step, scheduled for 30 simulation seconds.

Exemplary sectional views of the approximated drag, lift and pressure drop time profiles for three consecutive mesh refinement levels and a time step size of $\Delta t = 1/400$ are presented in Figure 12. Note that the depicted time interval is chosen arbitrarily after the drag and lift profiles were considered fully developed. In addition, the curves have been shifted in time in order to facilitate comparison.

Tables 6 and 7 supply minimum, maximum, mean, and amplitude values for the approximated drag and lift coefficients of different mesh refinement levels.

Level	Δt	\min - $C_D(\text{Abs-Err},\%\text{-Err})$	\max - $C_D(\text{Abs-Err},\%\text{-Err})$	mean- $C_D(Abs-Err,\%-Err)$	$\operatorname{amp-}C_D(\operatorname{Abs-Err},\%\operatorname{-Err})$
L4	1/400	3.2216 (0.0573, 1.81)	3.2857 (0.0583, 1.81)	$3.2536 \ (0.0578, 1.81)$	0.0642 (0.0011, 1.62)
L5	1/400	$3.1755 \ (0.0112, 0.35)$	$3.2392 \ (0.0118, \ 0.37)$	$3.2074 \ (0.0116, \ 0.36)$	$0.0637 \ (0.0006, \ 0.94)$
L6	1/400	$3.1665 \ (0.0022, 0.07)$	$3.2300 \ (0.0026, \ 0.08)$	$3.1983 \ (0.0025, 0.08)$	$0.0635 \ (0.0004, \ 0.58)$
Ref. [10]		3.1643	3.2274	3.1958	0.0631

Table 6: min, max, mean, and amplitude of the drag coefficient values (including their absolute and percent errors) for different mesh levels.

Our results are shown to converge to the most accurate available results of an alternative numerical simulation [10] using Q_2P_1 finite elements (without stabilization) for space discretization and Crank–Nicolson scheme for time discretization. Note that the absolute error of the lift coefficient is at level L4 already one order of magnitude smaller than that of the drag coefficient. However, the min/max values of the drag coefficient exhibit a significantly faster convergence than those of the lift coefficient.

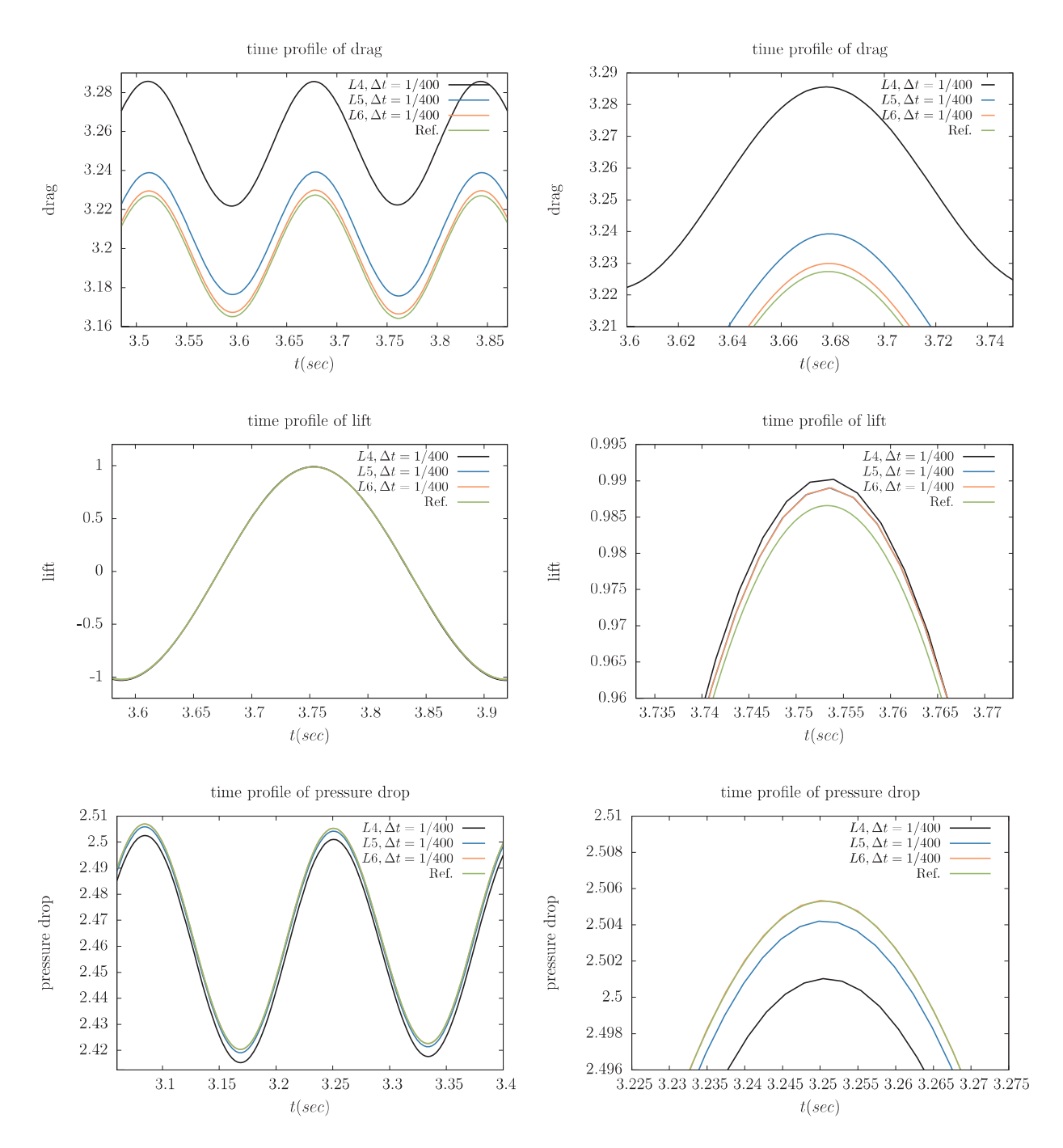


Figure 12: Sectional views of drag, lift, and pressure drop coefficient time profiles for Re 100 computed with a $\mathcal{S}_{0,0}^{3,3} \times \mathcal{S}_{0,0}^{2,2}$ discretization and a time step of $\Delta t = 1/400$. These profiles are shown to converge to $Q_2 P_1$ FE based reference [10] results. The numbers of degrees of freedom are given in Table 5.

Level	Δt	\min - $C_L(\text{Abs-Err},\%\text{-Err})$	\max - $C_L(Abs$ - Err ,%- Err)	mean- $C_L(\text{Abs-Err},\%\text{-Err})$	$\operatorname{amp-}C_L(\operatorname{Abs-Err}, \%\operatorname{-Err})$
L4	1/400	-1.0302 (0.0089, 0.87)	0.9903 (0.0037, 0.38)	-0.01995 (0.00259, 14.92)	2.0206 (0.0127, 0.63)
L5	1/400	-1.0249 (0.0036, 0.35)	$0.9890 \ (0.0024, \ 0.25)$	-0.01794 (0.00058, 3.34)	$2.0139 \ (0.0060, \ 0.30)$
L6	1/400	-1.0242 (0.0029, 0.28)	$0.9893 \ (0.0027, \ 0.27)$	-0.01747 (0.00011, 0.63)	$2.0135 \ (0.0056, \ 0.28)$
Ref. [10]		-1.0213	0.9866	-0.01736	2.0079

Table 7: min, max, mean, and amplitude of the lift coefficient values (including their absolute and percent errors) for different mesh levels.

In addition to min/max drag and lift coefficients, further quantities of interest are the lift profile frequency (f) and Strouhal number $(St = \frac{Df}{U})$ which we provide values for in Table 8.

Level	Δt	1/f	St
L4	1/400	0.33250	0.30075
L5	1/400	0.33250	0.30075
L6	1/400	0.33000	0.30303
Ref. [10]		0.33125	0.30189

Table 8: Frequency and Strouhal numbers for different mesh levels.

On a general note, different aspects of the approximated drag and lift profiles, such as their minimum, maximum, mean, frequency, and amplitude values are demonstrated to be converged and in good agreement with the results of a reference simulation.

6. Summary and conclusions

In this work, we have presented our numerical results of the application of Galerkin-based Isogeometric Analysis to both the steady and the unsteady incompressible Navier–Stokes equations in velocity–pressure formulation. The velocity and pressure functions were approximated with LBB stable B-spline spaces which can be regarded as smooth generalizations of Taylor–Hood pairs of finite element space.

The classical lid-driven cavity flow and flow around cylinder scenarios were considered in two dimensions as model problems in order to investigate the numerical traits and behavior of the isogeometric discretizations.

Starting off with the lid-driven cavity flow problem including its regularized version, we have shown that the approximated flow attributes are very well comparable with reference results partially obtained with a highly accurate spectral (Chebyshev Collocation) method [4]. Moreover, we have extended our view to global quantities such as kinetic energy and enstrophy, and have provided results which are in very good agreement with reference results obtained with other approaches such as a Q_2P_1 finite element discretization [17] and a high order finite difference scheme utilized in [5].

In addition to lid-driven cavity flow, we extended the application of Galerkin-based Isogeometric Analysis to the prominent flow around cylinder benchmark, as proposed in [19], and analyzed the approximated drag and lift quantities with respect to accuracy and convergence. The usage of a \mathcal{C}^1 B-spline element pair turned out to be superior to its \mathcal{C}^0 counterpart in terms of the number of degrees of freedom required to gain a certain accuracy. We eventually turned our attention to the unsteady Re-100 flow around cylinder case involving the transient

form of the Navier-Stokes equations. The governing equations were discretized in time with a second order implicit time discretization scheme and finally solved in a fully coupled mode. The time profile of the approximated drag and lift coefficients were shown to converge to the results of a reference finite element simulation.

The efficient solution of the arising linear equation systems with iterative techniques such as, for instance, multigrid were out of the scope of this study and will therefore be addressed in a forthcoming publication.

Isogeometric Analysis proved for us to be a robust and powerful technology showcasing unique features. For Taylor–Hood-like B-spline elements we carried our analysis upon, it turned out to be just a matter of changing settings in a configuration file to set up a desired B-spline element of a specific degree and continuity. This is without any doubt a huge benefit when compared to usual finite elements where one needs to provide an implementation for each element type. Moreover, for B-spline/NURBS geometries – already exactly representing a computational domain on the coarsest level – the process of meshing is straightforward. The mathematical definition of a B-spline/NURBS already defines a tensor product mesh eligible to NURBS-based refinement techniques such as h-, p-, or k-refinement [7, 18].

However, on a final note, the true virtue of the technology in the field of computational fluid dynamics can be better exploited in applications involving high order partial differential equations such as, for instance, the third order Navier–Stokes–Korteweg [14], or fourth order Cahn–Hilliard equations [13] in combination with complex geometries.

References

- [1] R.A. Adams and J.J.F. Fournier. *Sobolev Spaces*. Pure and Applied Mathematics. Elsevier Science, 2003.
- [2] F. Auricchio, L. Beirão Da Veiga, T.J.R. Hughes, A. Reali, and G. Sangalli. Isogeometric collocation methods. *Mathematical Models and Methods in Applied Sciences*, 20, No. 11:2075–2107, 2010.
- [3] Y. Bazilevs, L. Beirão Da Veiga, J.A. Cottrell, T.J.R. Hughes, and G. Sangalli. Isogeometric Analysis: Approximation, stability and error estimates for h-refined meshes. *Mathematical Models and Methods in Applied Sciences*, 16(7):1031–1090, 2006.
- [4] O. Botella and R. Peyret. Benchmark spectral results on the lid-driven cavity flow. Computers & Fluids, 27(4):421–433, 1998.
- [5] C.-H. Bruneau and M. Saad. The 2D lid-driven cavity problem revisited. Computers & Fluids, 35(3):326-348, 2006.
- [6] A. Buffa, C. De Falco, and G. Sangalli. IsoGeometric Analysis: Stable elements for the 2D Stokes equation. *International Journal for Numerical Methods in Fluids*, 65(11-12):1407–1422, 2011.
- [7] J.A. Cottrell, T.J.R. Hughes, and Y. Bazilevs. *Isogeometric Analysis: Toward Integration of CAD and FEA*. 2009.

- [8] J.A. Cottrell, T.J.R. Hughes, and A. Reali. Studies of refinement and continuity in isogeometric structural analysis. *Computer Methods in Applied Mechanics and Engineering*, 196(41-44):4160-4183, 2007.
- [9] J.A. Evans and T.J.R. Hughes. Isogeometric Divergence-conforming B-splines for the Steady Navier-Stokes Equations. *Mathematical Models and Methods in Applied Sciences*, 23(8):1421–1478, 2013.
- [10] http://www.featflow.de/en/benchmarks/cfdbenchmarking/flow/dfg_benchmark2_re100.html [Online; accessed 01-Oct-2014].
- [11] http://www.featflow.de/en/benchmarks/cfdbenchmarking/flow/dfg_benchmark_re20.html [Online; accessed 01-Oct-2014].
- [12] U. Ghia, K.N. Ghia, and C.T. Shin. High-Re Solutions for Incompressible Flow using the Navier-Stokes Equations and a Multigrid Method. *Journal of Computational Physics*, 48(3):387–411, 1982.
- [13] H. Gómez, V.M. Calo, Y. Bazilevs, and T.J.R. Hughes. Isogeometric Analysis of the Cahn-Hilliard phase-field model. Computer Methods in Applied Mechanics and Engineering, 197(49-50):4333-4352, 2008.
- [14] H. Gómez, T.J.R. Hughes, X. Nogueira, and V.M. Calo. Isogeometric analysis of the isothermal Navier-Stokes-Korteweg equations. Computer Methods in Applied Mechanics and Engineering, 199(25-28):1828–1840, 2010.
- [15] V. John. Higher order finite element methods and multigrid solvers in a benchmark problem for the 3D Navier–Stokes equations. *International Journal for Numerical Methods in Fluids*, 40(6):775–798, 2002.
- [16] G. Nabh. On High Order Methods for the Stationary Incompressible Navier-Stokes Equations. PhD thesis, University of Heidelberg, 1998.
- [17] M. Nickaeen, A. Ouazzi, and S. Turek. Newton multigrid least-squares FEM for the V-V-P formulation of the Navier-Stokes equations. *Journal of Computational Physics*, 256:416–427, 2014.
- [18] L.A. Piegl and W. Tiller. *The NURBS book.* Monographs in visual communication. Springer, 1995.
- [19] M. Schäfer, S. Turek, F. Durst, E. Krause, and R. Rannacher. Benchmark computations of laminar flow around a cylinder, January 1996.
- [20] D. Schillinger, J.A. Evans, A. Reali, M.A. Scott, and T.J.R. Hughes. Isogeometric collocation: Cost comparison with galerkin methods and extension to adaptive hierarchical nurbs discretizations. Computer Methods in Applied Mechanics and Engineering, 267:170–232, 2013.

- [21] A. Tagliabue, L. Dedè, and A. Quarteroni. Isogeometric Analysis and Error Estimates for High Order Partial Differential Equations in Fluid Dynamics. *Computers & Fluids*, 102:277–303, 2014.
- [22] S. Turek. Efficient Solvers for Incompressible Flow Problems An Algorithmic and Computational Approach, volume 6 of Lecture Notes in Computational Science and Engineering. Springer, 1999.
- [23] S. Turek, A. Ouazzi, and J. Hron. On pressure separation algorithms (PSepA) for improving the accuracy of incompressible flow simulations. *International Journal for Numerical Methods in Fluids*, 59(4):387–403, 2009.